

Weak Lensing Reveals a Tight Connection Between Dark Matter Halo Mass and the Distribution of Stellar Mass in Massive Galaxies

Song Huang^{1,2*}, Alexie Leauthaud¹, Andrew Hearin³, Peter Behroozi⁴,
Christopher Bradshaw¹, Felipe Ardila¹, Joshua Speagle⁵, Ananth Tenneti⁶,
Kevin Bundy⁷, Jenny Greene⁸, Cristóbal Sifón⁸, Neta Bahcall⁸

¹Department of Astronomy and Astrophysics, University of California Santa Cruz, 1156 High St., Santa Cruz, CA 95064, USA

²Kavli-IPMU, The University of Tokyo Institutes for Advanced Study, the University of Tokyo (Kavli IPMU, WPI), Kashiwa 277-8583, Japan

³Argonne National Laboratory, Argonne, IL 60439, USA

⁴Department of Astronomy and Steward Observatory, University of Arizona, Tucson, AZ 85721, USA

⁵Department of Astronomy, Harvard University, 60 Garden St, MS 46, Cambridge, MA 02138, USA

⁶McWilliams Center for Cosmology, Department of Physics, Carnegie Mellon University, Pittsburgh, PA 15213, USA

⁷UCO/Lick Observatory, University of California, Santa Cruz, 1156 High Street, Santa Cruz, CA 95064, USA

⁸Department of Astrophysical Sciences, Peyton Hall, Princeton University, Princeton, NJ 08540, USA

Accepted XXX. Received YYY; in original form ZZZ

ABSTRACT

Using deep images from the Hyper Suprime-Cam (HSC) survey and taking advantage of its unprecedented weak lensing capabilities, we reveal a remarkably tight connection between the stellar mass distribution of massive central galaxies and their host dark matter halo mass. Massive galaxies with more extended stellar mass distributions tend to live in more massive dark matter haloes. We explain this connection with a phenomenological model that assumes, (1) a tight relation between the halo mass and the total stellar content in the halo, (2) that the fraction of *in situ* and *ex situ* mass at $r < 10$ kpc depends on halo mass. This model provides an excellent description of the stellar mass functions (SMF) of total stellar mass (M_{\star}^{\max}) and stellar mass within inner 10 kpc (M_{\star}^{10}) and also reproduces the HSC weak lensing signals of massive galaxies with different stellar mass distributions. The best-fit model shows that halo mass varies significantly at fixed total stellar mass (as much as 0.4 dex) with a clear dependence on M_{\star}^{10} . Our two-parameter $M_{\star}^{\max} - M_{\star}^{10}$ description provides a more accurate picture of the galaxy–halo connection at the high-mass end than the simple stellar–halo mass relation (SHMR) and opens a new window to connect the assembly history of halos with those of central galaxies. The model also predicts that the *ex situ* component dominates the mass profiles of galaxies at $r < 10$ kpc for $\log M_{\star} \geq 11.7$. The code used for this paper is available online [🔗](#)

Key words: galaxies: elliptical and lenticular, cD – galaxies: formation – galaxies: haloes – gravitational lensing: weak

1 INTRODUCTION

During the last decade, observations and hydrodynamic simulations have significantly furthered our understanding of the formation of massive galaxies. The observed gradual mass assembly (e.g. Lundgren et al. 2014; Owsnworth et al.

2014; Bundy et al. 2017) and dramatic structural evolution (e.g. van der Wel et al. 2014; Clauwens et al. 2017; Hill et al. 2017) of massive galaxies support a ‘two-phase’ scenario for their formation. (e.g. Oser et al. 2010, 2012; Rodriguez-Gomez et al. 2016). Under this picture, intense dissipative processes at high-redshift swiftly builds up the massive, compact ‘core’ of today’s massive galaxies (e.g. Damjanov et al. 2009; Toft et al. 2014; van Dokkum et al. 2015), including

* E-mail: shuang89@ucsc.edu (SH)

most of the *in situ* component: stars formed in the main progenitor of the host dark matter halo (e.g. De Lucia & Blaizot 2007; Genel et al. 2009). Super massive galaxies, however, are also expected to have a large *ex situ* component: stars that are accreted from other haloes. After the quenching of star formation in massive galaxies, (e.g. Hopkins et al. 2008; Johansson et al. 2009; Conroy et al. 2015), the gradual accumulation of the *ex situ* component dominates the assembly of massive galaxies and helps build up extended stellar envelopes (e.g. van Dokkum et al. 2008; Bezanson et al. 2009; Patel et al. 2013; Huang et al. 2013). More importantly, these two components should show differences in their spatial distributions as a large fraction of the *ex situ* component is expected to be deposited at large radii (e.g. Hilz et al. 2013; Oogi & Habe 2013). This suggests that the stellar mass distribution of massive galaxies contains information about their assembly history.

From a cosmological perspective, to understand the assembly of massive galaxies is to understand how they hierarchically grow with their dark matter haloes (e.g. Wechsler & Tinker 2018 and the references within). Recently, the basic understanding of the stellar–halo mass relation (SHMR) has been established using various direct and indirect methods (e.g. Hoekstra 2007; More et al. 2011; Leauthaud et al. 2012a; Behroozi et al. 2013b; Coupon et al. 2015; Zu & Mandelbaum 2015; van Uitert et al. 2016; Tinker et al. 2017; Shan et al. 2017; Kravtsov et al. 2018). At low redshift, the SHMR can be characterized by a power-law relation at low masses, a characteristic pivot halo mass, and an exponential rise at higher masses (Behroozi et al. 2013b; Rodríguez-Puebla et al. 2017; Moster et al. 2018). Constraints on the SHMR have helped us gain insight into the galaxy–halo connection, but an in-depth picture about how the assembly of galaxies is tied to their dark matter haloes is still lacking. At high-mass end, the situation is particularly true (e.g. Tinker et al. 2017; Kravtsov et al. 2018). First, challenges in measuring the total stellar mass of massive elliptical galaxies with extremely extended light profile (e.g. Bernardi et al. 2013, 2014, 2017; Huang et al. 2018c; Kravtsov et al. 2018; Pillepich et al. 2018a) complicate constraints of the SHMR for massive galaxies. More importantly, this simple scaling relation does not provide the full picture; specifically, it does not describe whether or not the internal structure (i.e., the way in which stellar mass is distributed in massive galaxies) is tied to the assembly history of their dark matter haloes. At high stellar mass (M_\star) end, the scatter of halo mass at fixed stellar mass is of order 0.3–0.4 dex (e.g., Tinker et al. 2017). In this paper, we seek to explain how similarly massive galaxies can live in haloes with very different mass and assembly histories, by looking for signatures of this assembly process in the stellar mass profiles of massive galaxies.

In previous work (Huang et al. 2018c, Huang et al. 2018a; Paper I and Paper II hereafter), we map the stellar mass distributions of massive galaxies at $0.3 \leq z < 0.5$ to > 100 kpc individually using deep images from the Hyper Suprime-Cam (HSC; Miyazaki et al. 2012) Subaru Strategic Program (SSP, hereafter ‘HSC survey’; Aihara et al. 2017a,b). With the help of deep images and the redMaP-Per cluster catalog (e.g. Rykoff et al. 2014; Rozo & Rykoff 2014), we find evidence that the surface stellar mass density profiles (μ_\star) of massive central galaxies depend on dark matter halo mass: centrals galaxies in more massive halos

tend to have more extended stellar mass distributions (also see: Charlton et al. 2017; Yoon et al. 2017) and less mass in the inner 10 kpc (M_\star^{10}).

Here we seek to directly confirm this dependence and characterize this relation using the galaxy–galaxy weak lensing (‘g–g lensing’) method (e.g. Mandelbaum et al. 2006a,b; Leauthaud et al. 2012a; Coupon et al. 2015; Leauthaud et al. 2017) that probes the dark matter halo mass distribution by measuring the coherent shape distortion of background galaxies. Instead of relying on a cluster catalog, the unprecedented g–g lensing capability of the HSC survey (e.g. Mandelbaum et al. 2018; Medezinski et al. 2018; Miyatake et al. 2018) allows us to map the halo mass trend across a 2–D plane described by the M_\star^{10} and stellar mass within the largest aperture that is allowed by the depth of the image (M_\star^{\max}) and build an empirical model for galaxy–halo connection at high-mass end.

This paper is organized as follows. We briefly summarize the sample selection and data reduction processes in §2. Please refer to Paper I for more technical details. §3 describes the weak lensing methodology, and the measurements of aperture M_\star and μ_\star profiles are discussed in §4. In §5, we introduce an empirical model to describe the relation between dark matter halo mass and the distribution of stellar mass within super massive galaxies. The results from our best-fit model are presented in §6 and discussed in §7. Our summary and conclusions are presented in §8.

All magnitudes in this work are in AB system (Oke & Gunn 1983) and have been corrected for Galactic extinction using Schlafly & Finkbeiner (2011). For cosmology, we assume $H_0 = 70$ km s $^{-1}$ Mpc $^{-1}$, $\Omega_m = 0.3$, and $\Omega_\Lambda = 0.7$. Stellar mass (M_\star) is derived using a Chabrier initial mass function (IMF; Chabrier 2003). And we use the virial mass for dark matter halo mass (M_{vir}) as defined in Bryan & Norman 1998.

2 DATA AND SAMPLE SELECTION

2.1 SSP S16A data

In this work, we use the WIDE layer of the internal data release S16A of the HSC SSP, an ambitious imaging survey using the new prime focus camera on the 8.2-m Subaru telescope. These data are reduced by hscPipe 4.0.2, a specially tailored version of the Large Synoptic Survey Telescope (LSST) pipeline (e.g. Jurić et al. 2015; Axelrod et al. 2010), modified for HSC (Bosch et al. 2017). The coadd images are ~ 3 – 4 mag deeper than SDSS (Sloan Digital Sky Survey; e.g. Abazajian et al. 2009; Aihara et al. 2011; Alam et al. 2015), with a pixel scale of $0''.168$. The seeing in the *i*-band has a mean full width at half maximum (FWHM) of $0''.58$. Please refer to Aihara et al. (2017a,b) for more details about the survey design and the data products. The general performance of hscPipe is validated using a synthetic object pipeline synpipe (e.g. Huang et al. 2018b; code available on GitHub at this link [🔗](#)). In addition to the full-color and full-depth cuts, regions that are affected by bright stars are also masked out Coupon et al. (2017).

The HSC collaboration compiles the spectroscopic redshifts (spec- z hereafter) of HSC galaxies from a series of available spectroscopic surveys, which is the main sources of spec- z in this work. We also include additional spec- z

from the most recent data release of the [Galaxy And Mass Assembly](#) (GAMA) survey (Driver et al. 2009, 2011; Liske et al. 2015; Baldry et al. 2018) which significantly overlaps with HSC coverage in their G02, G09, G12, and G15 regions and greatly improve the spec- z completeness of our massive galaxy sample. The HSC collaboration also provides photometric redshift (photo- z hereafter) measurements using the point spread function (PSF)-matched five-band fluxes within $1''.5$ apertures and six different algorithms. Here, we use the spec- z sample and the photo- z measurements based on the [Flexible Regression over Associated Neighbors with Kernel density estimationN for Redshifts](#) (FRANKEN-Z; Speagle et al. in prep.) algorithm. Please refer to Tanaka et al. (2018) for details about photo- z catalogues.

For our weak lensing measurements, we make use of the first-year shear catalogue described in detail by Mandelbaum et al. (2018). Currently, we use the re-Gaussianization algorithm (Hirata & Seljak 2003) to measure galaxy shapes on i -band coadd images. Please see Mandelbaum et al. (2018) and Mandelbaum et al. (2017) for more details about our shape measurements and their calibration. Our shape catalogue also excludes a small fraction of the survey area that has a problematic PSF model. The resulting survey area is the full-depth full-color region for weak lensing analysis (WLFDFC) region, which covers ~ 137 deg 2 in all five bands (*grizy*) to the required imaging depth (5σ point source detection limit of 26.0 mag). For our g-g lensing measurements, we also use a random catalogue that contains a half million objects and covers the WLFDFC area (e.g. Singh et al. 2017; Coupon et al. 2017).

2.2 Sample selection

Our sample selection is very similar to Huang et al. (2018c) and Huang et al. (2018a) (Paper I and Paper II hereafter). We select all galaxies with $i_{\text{CModel}} \leq 22.0$ mag and useful five-band cModel photometry in the WLFDFC area. Instead of only using galaxies with spec- z 's however, we now assign a best redshift (z_{best}) to each object: We adopt the spec- z when it is available; for others, we use the photo- z measurements from FRANKEN-Z as z_{best} . We select all galaxies within $0.19 < z_{\text{best}} < 0.51$, where redshift evolution is not a serious concern and the volume is large enough (1.03×10^8 Mpc 3) to ensure a large sample of massive galaxies. The performance of FRANKEN-Z at this redshift and magnitude range is unbiased and reliable with respect to the training sample. The typical 1σ uncertainty is ~ 7 per cent with a median bias of about -0.3 per cent and typical outlier fraction of 11 to 19 per cent in this redshift range. Compared with the spec- z -only sample, adding in the photo- z 's greatly improves the M_{\star} completeness of our sample but does not alter any of our key results.

We perform five-band spectral energy distribution (SED) fitting using the cModel photometry to derive the average mass-to-light ratio (M_{\star}/L_{\star}) of galaxies and initial estimates of M_{\star} (M_{\star}^{cmod}). The SED fitting procedure is identical to the one used in Paper I. In short, we use [iSED-Fit](#) (Moustakas et al. 2013) to measure M_{\star}/L_{\star} ratios and k -corrections, assuming the Chabrier (2003) IMF and using the [Flexible Stellar Population Synthesis models](#) (FSPS; v2.4; Conroy & Gunn 2010a, Conroy & Gunn 2010b). Please refer to Paper I for more details. Based on the SED fitting

results, we select galaxies with $\log_{10}(M_{\star, \text{cmodel}}/M_{\odot}) > 10.8$ as the initial sample of massive galaxies. Typical uncertainty of M_{\star}^{cmod} is around 0.05 to 0.1 dex. We further measure the μ_{\star} profiles of these galaxies and aperture M_{\star} within different radii (see 4.1).

3 GALAXY-GALAXY WEAK LENSING METHODOLOGY

Galaxy-galaxy lensing measures the coherent shape distortion of background galaxies around foreground lens galaxies. Please refer to Mandelbaum et al. (2018) for a detailed description of the construction of our shear catalogue. A detailed description of our method for computing $\Delta\Sigma$ is presented in Speagle et al. in prep. Our methodology is briefly summarized below.

The HSC shape catalogue includes a per-galaxy optimal weight defined as

$$w_i = \frac{1}{e_{\text{rms}}^2 + \sigma_{e,i}^2} \quad (1)$$

where $\sigma_{e,i}$ is the shape measurement error per source galaxy and e_{rms} is the intrinsic shape noise.

We follow the methodology outlined in Singh et al. (2017) to measure the excess surface mass density (hereafter $\Delta\Sigma$) profiles of lens galaxies. Using this method, we measure $\Delta\Sigma$ as:

$$\Delta\Sigma_{\text{LR}}(r) = \frac{\Sigma_{L_s} w_{L_s} \gamma_t^{(L_s)} \Sigma_{\text{crit}}^{(L_s)}}{\Sigma_{L_s} w_{L_s}} - \frac{\Sigma_{R_s} w_{R_s} \gamma_t^{(R_s)} \Sigma_{\text{crit}}^{(R_s)}}{\Sigma_{R_s} w_{R_s}} \quad (2)$$

where we use L for a real-lens galaxy and R for random point. The superscript or subscript L_s indicates measurement for lens-source pair, while R_s means the measurement for random-source pair. γ is the tangential shear, w is the weight, and Σ_{crit} is the critical surface density defined as:

$$\Sigma_{\text{crit}} = \frac{c^2}{4\pi G} \frac{D_A(z_s)}{D_A(z_l) D_A(z_l, z_s) (1+z_l)^2} \quad (3)$$

where $D_A(z_L)$, $D_A(z_s)$, and $D_A(z_L, z_s)$ are the angular diameter distances to lens (random), source, and between them, respectively. We use 11 radial bins uniformly spaced in log-space from 200 kpc to 10 Mpc (physical units are assumed). The redshift distribution of random points is matched to the lens sample.

The subtraction of signal around random positions helps remove overestimated jackknife errors (e.g. Clampitt et al. 2017; Shirasaki et al. 2017) and accounts for non-negligible coherent additive bias of the shear measurements (e.g. Takada & Hu 2013). This method has been adopted by the Dark Energy Survey (DES; e.g. Prat et al. 2017) and the Kilo-Degree Survey (KiDS; e.g. Amon et al. 2018).

We selected source galaxies based on the following criteria. First, a set of photo- z quality cuts are applied to the sample; these are the basic cuts that are described in Speagle et al. (in prep.). For each lens, we further require $z_s - z_L \geq 0.1$ and $z_s > z_L + \sigma_{s,68}$, where $\sigma_{s,68}$ is the 1σ confidence interval of the source photo- z .

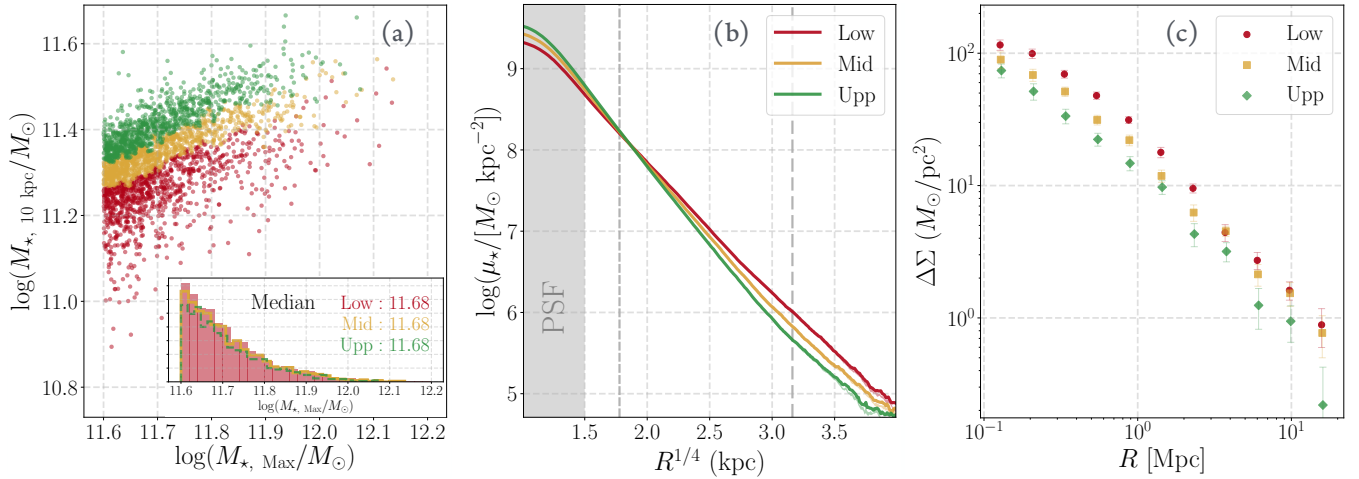


Figure 1. (a) Distribution of massive galaxies on the aperture mass plane. We group massive galaxies into three subsamples based on the ranking of their M_{\star}^{10} at fixed M_{\star}^{\max} . The inset plot demonstrates that the three subsamples share similar distributions of M_{\star}^{\max} . (b) Median surface mass density profiles of the subsamples visualize the differences in their stellar mass distributions. The x-axis employs a $R^{1/4}$ scaling. The shaded region within ~ 5 kpc highlights the region affected by seeing. Two dashed lines label the 10 kpc (short) and 100 kpc (long) radius. (c) The stacked g - g lensing signals prove that at fixed M_{\star}^{\max} , massive galaxies with lower M_{\star}^{10} tend to live in more massive dark matter haloes. The `Jupyter` notebook for this figure is available here: [🔗](#)

Errors are estimated via jackknife resampling. We divide the S16A WLFDFC footprint into 41 roughly equal-area jackknife regions with regular shapes. In practice, the effective number of jackknife regions varies, depending on the specific subsample of lenses. Typically $N_{\text{JK}} > 30$. The diagonal errors for $\Delta\Sigma$ are then estimated as:

$$\text{Var}_{\text{JK}}(\widehat{\Delta\Sigma}) = \frac{N_{\text{JK}} - 1}{N_{\text{JK}}} \sum_{i=1}^{N_{\text{JK}}} (\Delta\Sigma_i - \overline{\Delta\Sigma})^2 \quad (4)$$

where N_{JK} is the number of jackknife regions, $\Delta\Sigma_i$ is the $\Delta\Sigma$ profile in each region, and $\overline{\Delta\Sigma}$ is the mean profile among all jackknife regions.

We measure the stacked $\Delta\Sigma$ profiles of massive galaxies using a pure Python g - g lensing pipeline designed for the HSC survey: `dsigma` (available here: [🔗](#)). Please refer to Speagle et al. in prep. for more technical details of `dsigma` and the g - g lensing measurements.

4 MEASUREMENTS

4.1 μ_{\star} profiles and aperture stellar masses

We measure 1-D surface brightness profiles along the major axis of massive galaxies using HSC i -band images which typically have the best imaging conditions. We apply an empirical background correction and adaptively mask out neighbouring objects based on their brightness and distance to the target. At a given radius, we use the median intensity after 3σ -clipping along an elliptical isophote twice to measure the surface brightness level¹. Using the average M_{\star}/L_{\star}

measured from SED fitting, we then convert these profiles into surface density profiles of stellar mass – denoted μ_{\star} . Integration of the μ_{\star} profiles provides us with M_{\star} within an elliptical aperture. Paper I contains more technical details about our procedure.

We can reliably derive μ_{\star} profiles out to more than 100 kpc for individual massive galaxies without being limited by the background subtraction. On small scales, our profiles are resolved down to ~ 5 – 6 kpc^2 .

In Paper I and Paper II, we use M_{\star} within 10 kpc (M_{\star}^{10}) and 100 kpc (M_{\star}^{100}) as measures of the inner and ‘total’ M_{\star} of a galaxy. We also show that M_{\star}^{10} can be used as a rough proxy for the mass of the *in situ* component. In this work, instead of continuing to use M_{\star}^{100} , we choose to use the maximum 1-D stellar mass (M_{\star}^{\max}) as a proxy of ‘total’ M_{\star} . This choice integrates the μ_{\star} profile to the radius where the median intensity is consistent with the standard deviation of the sky background. We have shown that M_{\star}^{\max} on average adds another 0.03 to 0.05 dex of M_{\star} compared with M_{\star}^{100} ; hence, this approach should bring us a little closer to the true ‘total’ M_{\star} . This choice is motivated by the assumption of the empirical model but does not change the key results of this work, which we explain in §5.

As was the case in Paper I, we cannot derive 1-D profiles for ~ 11 per cent of massive galaxies due to strong contamination (e.g. a bright star or foreground galaxy) or complex inner structure (e.g. on-going major merger)³. Meanwhile, as shown in Huang et al. (2018b), `hscPipe` tends to classify some stars as extended objects. We find that these contaminations can be easily picked up as outliers on the M_{\star}^{100} - M_{\star}^{10} plane and removed using

¹ We use projected 2-D stellar mass maps from hydro-simulation to show that our profiles are robust against the impact of un-masked flux from other objects (Ardilla et al. in prep).

² $1.0''$ corresponds to 3.2 and 6.17 kpc at $z = 0.19$ and 0.51, respectively; while the mean i -band seeing has FWHM = $0''.58$.

³ The M_{\star}^{mod} distribution of these galaxies is similar to the whole sample; hence, excluding them should not bias our model.

$\log(M_{\star,\text{tot}}/M_{\odot}) - \log_{10}(M_{\star,10\text{kpc}}/M_{\odot}) \leq 0.03$. In this work we ignore the M_{\star}/L_{\star} gradients. Based on [Roediger & Courteau \(2015\)](#)⁴, a color difference of $\Delta(g-i) = 0.2$, which is roughly the average $g-i$ color difference between 10 to 100 kpc, translates into a M_{\star}/L_{\star} difference of $\Delta \log(M_{\star}/L_i) \sim 0.15$. Considering that the cModel photometry measures the average color for the main body of massive galaxies, we believe that the systematic uncertainty caused by ignoring the color gradient should be smaller than this value. Assuming a negative color gradient, we may be slightly underestimating M_{\star}^{10} while slightly overestimating M_{\star}^{max} .

Our sample contains 38,653 galaxies with $\log_{10}(M_{\star,\text{max}}/M_{\odot}) \geq 11.0$ at $0.19 \leq z \leq 0.51$. Fifty-seven per cent of them have $\text{spec-}z$'s.

4.2 Stellar mass functions

In this work, we estimate the stellar mass function (SMF) of M_{\star}^{max} (Φ_{max}) in seven bins between $11.6 \leq \log_{10}(M_{\star,\text{max}}/M_{\odot}) < 12.3$, while we estimate the SMF of M_{\star}^{10} (Φ_{10}) in ten bins between $10.8 \leq \log_{10}(M_{\star,10\text{kpc}}/M_{\odot}) < 11.8$. We separate the current WLFDFC area into 30 smaller regions, and derive uncertainties via jackknife resampling. We add a 10 per cent uncertainty to represent the potential impact of galaxies without a useful 1-D profile. We take the uncertainty of M_{\star} measurements into account by integrating the normalized posterior distribution function (PDF) of the M_{\star} of each galaxy⁵ to estimate its contribution in each M_{\star} bin. For a given M_{\star} bin with lower and upper boundary of M_l and M_u , the effective number of galaxies in the bin is:

$$N_{\text{eff}} = \sum_{i=1}^{n_{\text{gal}}} \frac{1}{2} \left[\text{erf}\left(\frac{M_u - M_i}{\sqrt{2}\sigma_i}\right) - \text{erf}\left(\frac{M_l - M_i}{\sqrt{2}\sigma_i}\right) \right] \quad (5)$$

where M_i is the mean M_{\star} and σ_i is the uncertainty for each massive galaxy and $\text{erf}()$ is the error function.

By comparing our results with SMFs from the PRIMUS Multi-object Survey ([PRIMUS](#); e.g. [Moustakas et al. 2013](#)) at a similar redshift, we find that massive galaxies with $\log_{10}(M_{\star,\text{max}}/M_{\odot}) \geq 11.6$ are a mass complete sample and are considered in the following modelling. In total, we have **6481 and 3156 galaxies** at $\log_{10}(M_{\star,\text{max}}/M_{\odot}) \geq 11.5$ and ≥ 11.6 ; **5756 and 2944** of them have $\text{spec-}z$. The $M_{\star}^{\text{max}}-M_{\star}^{10}$ distribution of our sample is shown in [Figure 1](#) and [Figure 4](#). The SMFs of M_{\star}^{max} and M_{\star}^{10} for the $\log_{10}(M_{\star,\text{max}}/M_{\odot}) \geq 11.6$ sample are shown in panel (b) of [Figure 4](#).

The SMFs of M_{\star}^{max} and M_{\star}^{10} are highly correlated as M_{\star}^{10} is included in the measurement of M_{\star}^{max} . We calculate the covariance matrix of the joint $M_{\star}^{\text{max}}-M_{\star}^{10}$ SMF using the same jackknife samples.

4.3 Galaxy-galaxy lensing signals across the aperture mass plane

In [Paper II](#) (see [Figure 3](#)), we find that massive central galaxies of redMaPPer clusters (e.g. [Rykoff et al. 2014](#); [Roza](#)

& [Rykoff 2014](#)) have lower M_{\star}^{10} than those in less massive haloes at fixed M_{\star}^{100} , which suggests that the stellar mass distributions in massive central galaxies depend on their M_{vir} . Therefore, we expect a gradient of M_{vir} across the aperture mass plane. Our goal is to map out this gradient directly using weak lensing and without relying on any redMaPPer cluster catalog.

Panel (a) in [Figure 1](#) shows the distribution of massive galaxies over the $M_{\star}^{\text{max}}-M_{\star}^{10}$ plane. We group galaxies into three sub-samples based on the ranking of their M_{\star}^{10} at fixed M_{\star}^{max} , following a similar strategy employed in [Mao et al. \(2018\)](#). As illustrated in the inset panel, the three sub-samples share almost identical distributions of M_{\star}^{max} . Therefore, they represent massive galaxies with different stellar mass distributions at the same ‘total’ stellar mass, as proved by their median μ_{\star} profiles (panel (b) of [Figure 1](#)). Galaxies with lower M_{\star}^{10} have lower μ_{\star} on small radial scales and have larger extended outer envelopes. The median μ_{\star} profiles cross each other at $\sim 12-15$ kpc, close to the effective radius (R_e) of these galaxies.

We then measure the stacked $\Delta\Sigma$ profiles of these three sub-samples using the method described in [§3](#). The results are displayed in panel (c) of [Figure 1](#). It is very clear from this [Figure](#) that, on average, massive galaxies with lower M_{\star}^{10} have higher $\Delta\Sigma$ signals indicating that they live in more massive dark matter haloes. This confirms the expected trend across the aperture mass plane that was first identified in [Paper II](#) using broad M_{vir} bins from cluster catalog.

Thanks to the impressive weak lensing capabilities of the HSC survey, we can further group massive galaxies into bins of M_{\star}^{max} and M_{\star}^{10} and investigate the variation of their stacked $\Delta\Sigma$ profiles and halo masses. The [Jupyter](#) notebook for measuring these $\Delta\Sigma$ profiles can be found here: [📄](#). We also make a GIF animation to visualize this variation: [📺](#).

To account for scatter in M_{vir} within each $M_{\star}^{\text{max}}-M_{\star}^{10}$ ‘box’, the impact of satellites, and the two-halo term, we model our lensing signals using a full forward model based on N-body simulations and a state-of-the-art semi-empirical model. We will group our massive galaxies into 12 bins of aperture masses while making sure that (1) there are enough massive galaxies in each bin so that the stacked $\Delta\Sigma$ profile has good S/N; and (2) the M_{\star}^{10} bins at fixed M_{\star}^{max} represent massive galaxies with different stellar mass in the inner region. We explain the details of the model in [Section 5](#).

5 MODELLING THE $M_{\text{vir}}-M_{\star}^{\text{max}}-M_{\star}^{10}$ RELATION

5.1 Goals of the Model

Our goal is to construct a model that connects the hierarchical growth of dark matter halos to the assembly and structure of high mass central galaxies.

Ideally, we could directly compare with predictions from hydro-dynamical simulation, such as [Illustris](#) (e.g. [Vogelsberger et al. 2014](#); [Genel et al. 2014](#)) or [EAGLE](#) (e.g. [Schaye et al. 2015](#); [Crain et al. 2015](#)) that are being used to study the evolution of massive galaxies (e.g. [Wellons et al. 2016](#); [Rodríguez-Gomez et al. 2016](#); [Qu et al. 2017](#)). However, current hydro-simulations typically lack of the volume to study galaxies at high- M_{vir} end statistically. In addition, we also

⁴ $\log(M_{\star}/L_i) = 0.83 \times (g-i) - 0.597$ for the FSPS stellar population model

⁵ We assume that the PDF is described by a Gaussian distribution.

Symbol	Origin	Explanation
M_{\star}^{10}	Observation	Aperture M_{\star} within inner 10 kpc via integrating the 1-D μ_{\star} profile
M_{\star}^{\max}	Observation	Maximum aperture M_{\star} via integrating the 1-D μ_{\star} profile
M_{vir}	SMDPL	Dark matter halo mass within virial radius (Bryan & Norman 1998)
M_{peak}	SMDPL	Peak historical dark matter halo mass
M_{\star}^{all}	UniverseMachine	M_{\star} of all galaxies (central and satellites) within a host dark matter halo
M_{\star}^{gal}	UniverseMachine	M_{\star} of a central or satellite galaxy
M_{\star}^{cen}	UniverseMachine	M_{\star} of the central galaxy
M_{\star}^{ins}	UniverseMachine	M_{\star} of the <i>in situ</i> component of a galaxy
M_{\star}^{exs}	UniverseMachine	M_{\star} of the <i>ex situ</i> component of a galaxy
δ_{gal}	UniverseMachine	$M_{\star}^{\text{gal}}/M_{\star}^{\text{all}}$: stellar mass fraction of galaxy in the halo
δ_{ins}	UniverseMachine	$M_{\star}^{\text{ins}}/M_{\star}^{\text{gal}}$: stellar mass fraction <i>in situ</i> component in the galaxy
δ_{exs}	UniverseMachine	$M_{\star}^{\text{exs}}/M_{\star}^{\text{gal}}$: stellar mass fraction <i>ex situ</i> component in the galaxy
$\mathcal{M}_{\star}^{\text{all}}$	ASAP	Model predicted total M_{\star} in a host dark matter halo
$\mathcal{M}_{\star}^{\text{gal}}$	ASAP	Model predicted M_{\star} of a galaxy (central or satellite)
$\mathcal{M}_{\star}^{\text{cen}}$	ASAP	Model predicted M_{\star} of a central galaxy
$\mathcal{M}_{\star}^{\text{ins}}$	ASAP	Model predicted <i>in situ</i> M_{\star}
$\mathcal{M}_{\star}^{\text{exs}}$	ASAP	Model predicted <i>ex situ</i> M_{\star}
$\mathcal{M}_{\star}^{\text{in},10}$	ASAP	Model predicted <i>in situ</i> M_{\star} within inner 10 kpc
$\mathcal{M}_{\star}^{\text{ex},10}$	ASAP	Model predicted <i>ex situ</i> M_{\star} within inner 10 kpc
\mathcal{M}_{\star}^{10}	ASAP	Model predicted 10 kpc aperture M_{\star}

Table 1. Definitions of halo masses and stellar masses used in this work. Rows with different colors are used to separate the masses defined in observations (blue), in (SMDPL) dark matter simulation (orange), in the UniverseMachine model predictions (green), and in the Accelerated SAP (ASAP) model developed in this work (red). Notation with calligraphic letters is used to denote model predictions

want a model with the flexibility (free parameters) to fit the actual observations.

An alternative approach would be to use a semi-analytic model (SAM) based on dark matter simulations and approximate physical recipes (e.g. White & Frenk 1991; Benson & Bower 2010; Guo et al. 2011; Henriques et al. 2015; Somerville et al. 2015; Croton et al. 2016) could be another approach. However, while recent progress has been made in this area, fitting the large numbers of parameters that a SAM typically uses is still non trivial (e.g. Lu et al. 2011; Benson 2014, 2017).

For these reasons, we base our formalism on the recently developed semi-empirical model approach (e.g. Becker 2015; Rodríguez-Puebla et al. 2017; Moster et al. 2018; Behroozi et al. 2018). This new methodology makes rather minimal *a priori* assumptions about the galaxy–halo connection, and is constrained by observations at different redshifts (stellar mass growth, star-formation history, and clustering properties of galaxies across a wide range of halo masses and redshifts). This results in a model that can predict the properties of *individual galaxies* and how they connect with the full assembly history of their dark matter halos.

5.2 Simulations and UniverseMachine framework

UniverseMachine (Behroozi et al. 2018; code available here: [🔗](#)) is a massively parallel implementation of a semi-empirical modeling method. It is capable of reproducing key observations (e.g. stellar mass functions, star formation rates, and quenched fractions) over a large range of stellar masses and redshifts. For a given halo from a cosmological simulation, UniverseMachine parametrizes its star formation rate (SFR) as a function of halo mass, halo accretion rate, and redshift. UniverseMachine exploits the Markov Chain Monte Carlo (MCMC) Bayesian method to compare results with a series of compiled observations.

The UniverseMachine model we use here is based on the Small MultiDark Planck (SMDPL) simulation, which is part of the MultiDark simulation series using a Planck cosmology. It has a 400 Mpc/ h simulation box size and uses 3840^3 particles. The dark matter mass resolution is $10^8 M_{\odot}/h$. The volume of the SMDPL simulation is two times larger than the volume from which our HSC sample at $0.19 \leq z \leq 0.51$ is drawn from. Dark matter subhalo properties are extracted using the Rockstar (Behroozi et al. 2013a) halo finder with merger trees generated by the Consistent Trees code. Halo mass is defined as the mass within the virial radius (M_{vir}) using the formula from Bryan & Norman (1998). For satellite

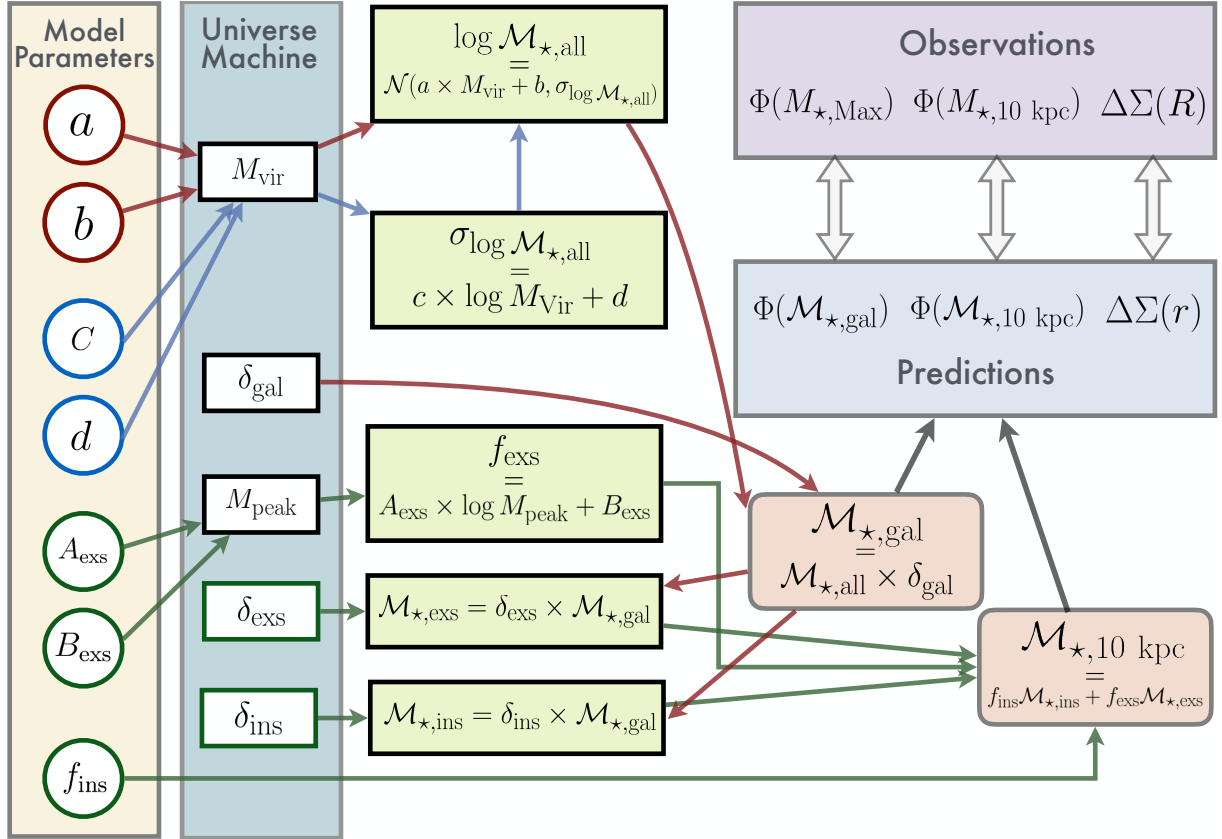


Figure 2. Flowchart for the basic design of the ASAP model. The **UniverseMachine** predictions adopted in this model are highlighted on the right. These correspond to: M_{peak} —the peak halo mass; δ_{gal} —the ratio between the stellar mass of a galaxy ($\mathcal{M}_{\star}^{\text{gal}}$) and the total stellar mass within the halo ($\mathcal{M}_{\star}^{\text{all}}$); also the fraction of *in situ* (δ_{ins}) and *ex situ* (δ_{exs}) components in the \mathcal{M}_{\star} of each galaxy. The seven free model parameters are labelled on the bottom: a and b describe a log–log linear relation between M_{peak} and \mathcal{M}_{\star} ; c and d describe a linear relation between the scatter of \mathcal{M}_{\star} and M_{peak} . These four parameters, along with the δ_{gal} fraction predicted by **UniverseMachine**, provide predictions of the stellar mass of each galaxy ($\mathcal{M}_{\star}^{\text{gal}}$) that will be compared with the observed $\mathcal{M}_{\star}^{\text{max}}$. The stellar mass of *in situ* and *ex situ* components ($\mathcal{M}_{\star}^{\text{ins}}$ and $\mathcal{M}_{\star}^{\text{exs}}$) are estimated using $\mathcal{M}_{\star}^{\text{gal}}$, δ_{ins} , and δ_{exs} . The predicted stellar mass in 10 kpc (\mathcal{M}_{\star}^{10}) requires another three free parameters; f_{ins} describes the fraction of *in situ* stars located within the inner 10 kpc, and the fraction of *ex situ* stars in 10 kpc follows a linear relation with $\log_{10} M_{\text{peak}}$ that is characterized by A_{ins} and B_{exs} . A keynote version of this flowchart is available here: [📄](#)

galaxies, we will also use their peak M_{vir} over their accretion history (M_{peak}). Here we use the snapshot at $z \sim 0.37$, which is very close to the mean redshift of our sample ($\bar{z} \sim 0.32$).

The fiducial **UniverseMachine** model predicts a ‘galaxy mass’ and an ‘ICL’ mass. During mergers, a fraction of stars from the incoming satellite become unbound by the gravitational well of the galaxy and are added to the ‘ICL’ component. Although there is evidence for an unbound diffuse stellar component around nearby massive galaxies (e.g. [Kelson et al. 2002](#); [Bender et al. 2015](#); [Longobardi et al. 2015](#)), the main motivation of this approach is to make sure the SMF matches observational constraints at low redshift, otherwise **UniverseMachine** over-produce the SMF at the high- \mathcal{M}_{\star} end ([Behroozi et al. 2018](#)). However, as we showed in [Paper I](#), it is extremely difficult to photometrically separate out a physically meaningful ‘ICL’ component. More importantly, the ICL component is also an integrated part of the assembly history of massive galaxies and should be taken into account when studying their galaxy–halo connection.

Therefore, instead of using the ‘galaxy’ and ‘ICL’ separation, we use a specially tailored **UniverseMachine** model

that provides a more physically motivated decomposition of stars in massive galaxies: for each galaxy, our **UniverseMachine** model will predict the mass of the *in situ* and *ex situ* components ($\mathcal{M}_{\star}^{\text{ins}}$ and $\mathcal{M}_{\star}^{\text{exs}}$). As mentioned earlier, these are stars formed inside and outside the *main progenitor* of the subhalo. For each galaxy, the stellar mass of the galaxy ($\mathcal{M}_{\star}^{\text{gal}}$) is simply the sum of $\mathcal{M}_{\star}^{\text{ins}}$ and $\mathcal{M}_{\star}^{\text{exs}}$. The stellar mass of the central galaxy in a halo is denoted as $\mathcal{M}_{\star}^{\text{cen}}$. For each halo, we also calculate the total stellar mass within the halo ($\mathcal{M}_{\star}^{\text{all}}$) meaning the sum of stellar mass of the central and *all* satellites. These stellar mass definitions are given in [Table 1](#).

5.3 ASAP model

In this section, we explain the design and key assumptions behind our empirical model, which we call the **ASAP**⁶ model.

⁶ An initialism for Alexie Leauthaud, Song Huang, Andrew Hearin, and Peter Behroozi, the first names of the main contributors.

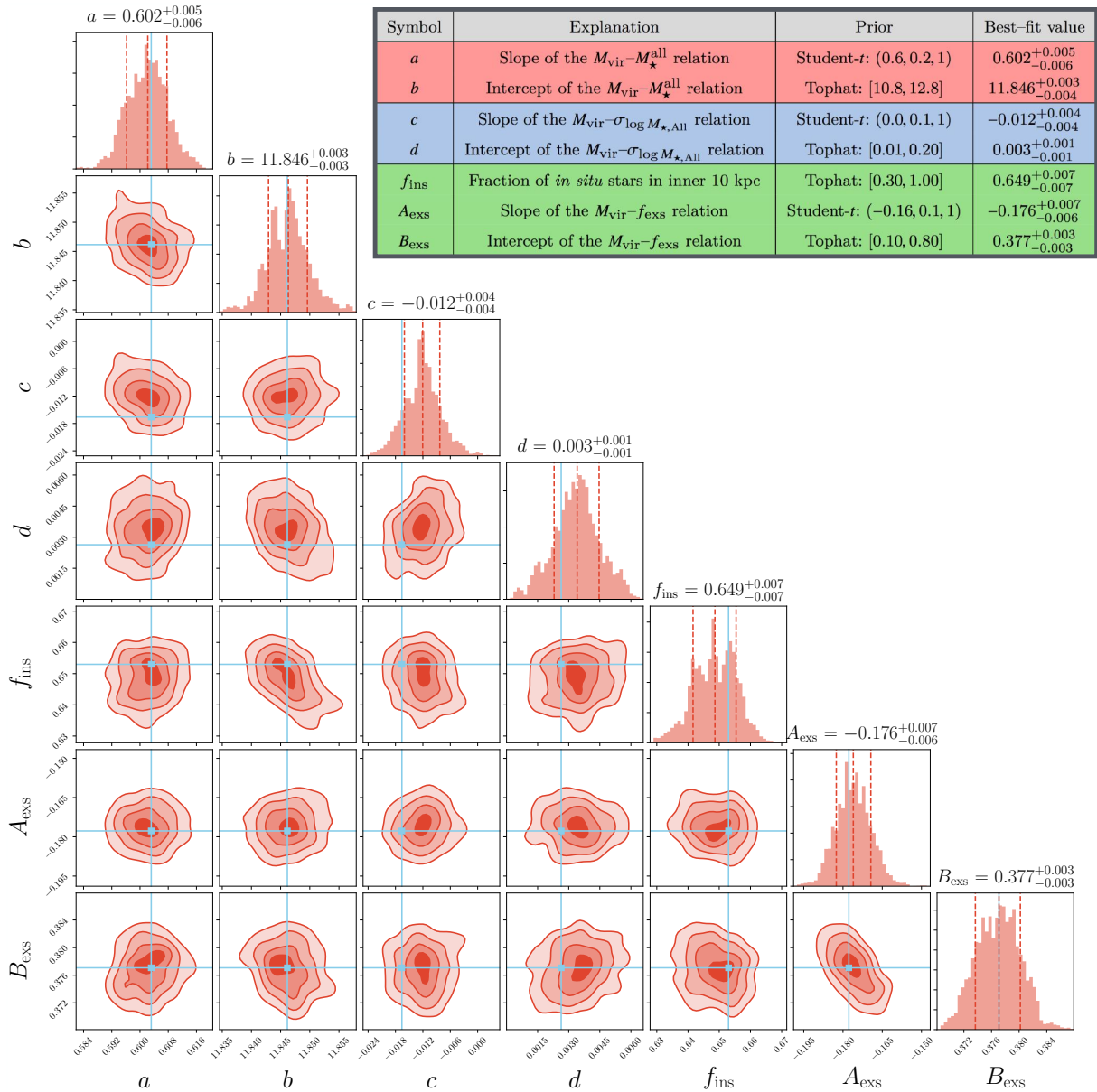


Figure 3. Corner plot for the posterior probability distributions of parameters in the model. The contour levels describe 68 per cent, 95 per cent, and 99.7 per cent enclosed probability regions. The explanations, ranges of uniform priors, and the best-fit values along with their uncertainties are highlighted in the upper-right table. The colors separate parameters into three groups as indicated in the flowchart. The **Jupyter** notebook for this figure is available here: [📄](#)

Constrained by the observed SMFs of different aperture masses and $\Delta\Sigma$ profiles across the aperture mass plane, the ASAP model will connect M_{vir} , M_{\star}^{ins} , and M_{\star}^{exs} to the observed stellar mass distributions among massive galaxies. The ASAP model is based on the following two key ingredients:

(i) There is a tight log–log linear relation between halo mass and the total stellar mass within the halo (TSHMR) at the high- M_{vir} end (Bradshaw et al in prep).

(ii) The **UniverseMachine** model provides *in situ* and *ex situ* components – we add a prescription to describe the spatial distributions of these components.

5.3.1 Total Stellar–Halo Mass Relation (TSHMR)

The SHMR is the relation between halo mass and central galaxy mass. Whereas the SHMR has an exponentially rising slope and large scatter at the high mass end, recent hydro-simulations (e.g. Pillepich et al. 2017) and semi-empirical models (e.g. Behroozi et al. 2018, Bradshaw et al. in prep.) suggest that the TSHMR follows the simple tight, log-linear correlation with M_{vir} (at least at the high- M_{vir} end). In observations, the total K s -band luminosity or stellar mass in galaxy groups and clusters also show tight relation with halo mass (e.g. Lin & Mohr 2004; Ziparo et al. 2016; Leauthaud et al. 2012b; van der Burg et al. 2014; Budzynski et al. 2014; Patel et al. 2015; Kravtsov et al. 2018). Motivated by this, we

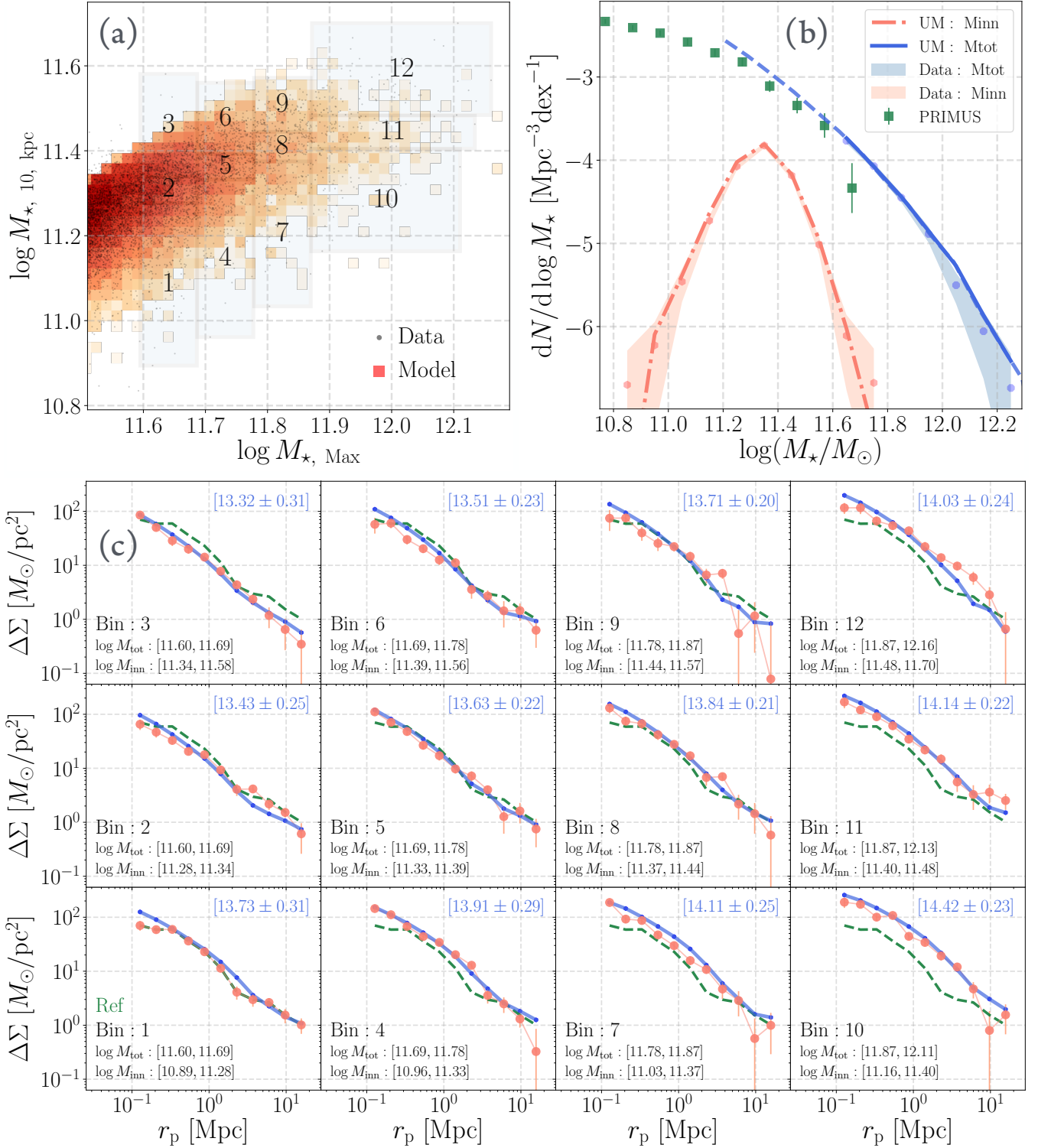


Figure 4. Performance of the best-fit model. (a) Comparison between the observed HSC galaxies (grey points) and modeled galaxies (density plot) over the $M_{\star}^{\text{max}}-M_{\star}^{10}$ plane. Both observed and modeled galaxies with $\log_{10}(M_{\star, \text{max}}/M_{\odot}) \geq 11.6$ are grouped into the same 12 bins using M_{\star}^{max} and M_{\star}^{10} values to compare the g-g lensing signals within each bin. (b) Comparisons of observed (dots and shaded regions) and modeled SMFs (solid lines) for M_{\star}^{max} (blue) and M_{\star}^{10} (red). We also overplot the SMF from the PRIMUS survey at similar redshift to show the shape of SMF at lower M_{\star} . (c) Comparisons of g-g lensing signals in each $M_{\star}^{\text{max}}-M_{\star}^{10}$ bin. The bin number and the mass range of M_{\star}^{max} and M_{\star}^{10} of each bin is given in the lower-left corner of each subplot. The observed g-g lensing signals are shown as red points, while the blue lines show the modeled lensing signal. The weak lensing signal from Bin = 1 (bottom-left plot) is shown in each subplot as a green dashed line to highlight the evolution of $\Delta\Sigma$ amplitudes across various bins. The median M_{vir} in each bin is shown in the upper-right corner of each subplot. The `Jupyter` notebook for this figure is available here: [🔗](#)

place the TSHMR at the core of our approach. The SHMR then emerges as a consequence of the TSHMR and the assembly histories of halos (e.g. Bradshaw et al. in prep.).

We assume a log-linear relation between the mass of the host dark matter halo (M_{vir}) and the total stellar mass within the halo (including the central galaxy, satellites from all subhaloes, and the ICL component; $\mathcal{M}_{\star}^{\text{all}}$). The TSHMR used in the ASAP model is described as:

$$\log \mathcal{M}_{\star}^{\text{all}} = a \times (\log M_{\text{vir}} - 13.5) + b \quad (6)$$

The slope (a) and intercept (b) are free parameters in our model. We adopt a pivot M_{vir} of $\log_{10}(M_{\text{vir}}/M_{\odot}) = 13.5$ in all log-linear scaling relations involving halo mass to reduce the degeneracy between the slope and intercept. The exact value of this pivot mass does not impact our results. The scatter in this relation is also modeled as a simple linear relation:

$$\sigma_{\log \mathcal{M}_{\star}^{\text{all}}} = c \times (\log M_{\text{vir}} - 13.5) + d \quad (7)$$

where c and d are two additional parameters. The above relations determine the total amount of \mathcal{M}_{\star} in each ‘parent’ halo in the ASAP model. We do not use the value of $\mathcal{M}_{\star}^{\text{all}}$ directly from the `UniverseMachine` because the current version of the `UniverseMachine` is constrained to match stellar mass functions from Muzzin et al. (2013) that contain larger numbers of massive galaxies (see Behroozi et al. 2018). We should point out that, when comparing to observations, the scatter should be a combination of the intrinsic scatter of the TSHMR and the measurement errors of observed stellar mass and weak lensing profiles. We will discuss the scatter of TSHMR further in §6.3.1.

So far, our model has simply ‘pasted’ $\mathcal{M}_{\star}^{\text{all}}$ values on halos in our simulations. The information that we adopt from the `UniverseMachine` is the following. The `UniverseMachine` model tells us, for a given $\mathcal{M}_{\star}^{\text{all}}$, how mass is divided up among galaxies. For every galaxy, we compute $\delta_{\text{gal}} \equiv \mathcal{M}_{\star}^{\text{gal}}/\mathcal{M}_{\star}^{\text{all}}$. At this stage, we also forward model uncertainties associated with stellar mass measurements. Thus, each galaxy in our mock is assigned a mass following:

$$\log \mathcal{M}_{\star, \text{gal}} \sim \mathcal{N}(\log(\mathcal{M}_{\star}^{\text{all}} \times \delta_{\text{gal}}), \sigma_{\log \mathcal{M}_{\star}^{\text{all}}}) \quad (8)$$

where $\mathcal{N}(\mu, \sigma)$ is a normal distribution with mean value of μ and standard deviation of σ .

We apply this model to both centrals and satellite galaxies. Massive satellites are included in our forward modeling process because we do not attempt to distinguish centrals and satellites in our HSC sample⁷.

5.3.2 Spatial distributions of *in situ* and *ex situ* stars

For every galaxy, the second ingredient that we inherit from the `UniverseMachine` is the fraction of *in situ* and *ex situ*

component (δ_{ins} and δ_{exs}). We now model the observed aperture masses, \mathcal{M}_{\star}^{10} and $\mathcal{M}_{\star}^{\text{max}}$, via a prescription that describes the spatial distributions of *in situ* and *ex situ* stars. First, we assume the observed $\mathcal{M}_{\star}^{\text{max}}$ is a good proxy for the ‘total’ stellar mass of the galaxy:

$$\mathcal{M}_{\star}^{\text{max}} = \mathcal{M}_{\star}^{\text{ins}} + \mathcal{M}_{\star}^{\text{exs}}. \quad (9)$$

Next, we predict \mathcal{M}_{\star}^{10} using two assumptions. First, we assume that a fixed fraction of the *in situ* component is within the inner 10 kpc of the galaxy:

$$\mathcal{M}_{\star}^{\text{in}, 10} = f_{\text{ins}} \times \mathcal{M}_{\star}^{\text{ins}}. \quad (10)$$

Second, we assume that the fraction of *ex situ* stars within 10 kpc depends on halo mass:

$$\mathcal{M}_{\star}^{\text{ex}, 10} = f_{\text{exs}} \times \mathcal{M}_{\star}^{\text{exs}} \quad (11)$$

where the relation between the fraction and halo mass is described by:

$$f_{\text{exs}} = A_{\text{exs}} \times (M_{\text{vir}} - 13.5) + B_{\text{exs}}. \quad (12)$$

Given these two assumptions, the predicted 10 kpc aperture mass is then: $\mathcal{M}_{\star}^{10} = \mathcal{M}_{\star}^{\text{in}, 10} + \mathcal{M}_{\star}^{\text{ex}, 10}$. To model \mathcal{M}_{\star}^{10} therefore requires three extra free parameters: f_{ins} , A_{exs} , and B_{exs} .

For satellite galaxies, we use M_{peak} instead of M_{vir} . However, because the fraction of satellite galaxies that are massive enough to be included in our sample is very low at the high stellar mass end (Sallaberry et al in prep), this choice has no impact on our results. As the scatter of the TSHMR is designed to carry both intrinsic scatter and measurement uncertainties of stellar mass, the predicted \mathcal{M}_{\star}^{10} and $\mathcal{M}_{\star}^{\text{Max}}$ will be described by normal distributions with the same scatter.

In total, our model has seven free parameters: two for the TSHMR; two for the scatter of the TSHMR; and three for the fraction of *in situ* and *ex situ* stars within 10 kpc. Figure 2 is a visualization of our model.

5.3.3 Predictions for the SMFs and $\Delta\Sigma$ profiles

We predict the SMFs of \mathcal{M}_{\star}^{10} and $\mathcal{M}_{\star}^{\text{Max}}$ using the same method and in the same stellar mass bins for the observed SMFs. Uncertainty in stellar mass measurements is accounted for according to equation (7).

When comparing the predicted and observed SMFs, we jointly constrain the Φ_{max} and Φ_{10} (referred to as Φ_{obs}) by taking the measured covariance matrix (\mathbf{C}_{obs}) into account. The log-likelihood for SMF is:

$$\ln \mathcal{L}_{\text{SMF}} = -\frac{1}{2} [\Phi_{\text{mod}} - \Phi_{\text{obs}}]^T \mathbf{C}_{\text{obs}}^{-1} [\Phi_{\text{mod}} - \Phi_{\text{obs}}] + K \quad (13)$$

where Φ_{mod} is the predicted SMFs for \mathcal{M}_{\star}^{10} and $\mathcal{M}_{\star}^{\text{Max}}$ aligned in the same order with the observed SMFs. K is a constant described by $-\frac{1}{2} [\ln(2\pi)N + \ln(\det(\mathbf{C}_{\text{obs}}))]$ and $N = 17$, which is the total number of mass bins.

The lensing observable, $\Delta\Sigma$, is computed directly from

⁷ Uncertainties of photometric redshifts make it difficult to accurately separate centrals and satellites. Meanwhile, the satellite fraction at $\log_{10}(M_{\star, \text{max}}/M_{\odot}) \geq 11.5$ is less than < 10 per cent; see Sallaberry et al. in prep.

the simulation using 50 million randomly selected dark matter particles and the `mock_observables.delta_sigma` function in the `halotools` (Hearin et al. 2017). We predict the weighted-mean $\Delta\Sigma$ profiles in the same 12 aperture mass bins used for observation for comparison after considering the uncertainties of the predicted \mathcal{M}_\star^{10} and $\mathcal{M}_\star^{\text{Max}}$ into the weight. Our method accounts for the effects of scatter, the finite width of our bins, satellite galaxies, and the two-halo term. We ignore the contribution of M_\star to $\Delta\Sigma$ because it is negligible on the scales that we consider ($r > 200$ kpc).

The log-likelihood for comparing $\Delta\Sigma$ profiles is described as:

$$\ln \mathcal{L}_{\Delta\Sigma_j} = -\frac{1}{2} \sum_i^n \frac{(\Delta\Sigma_{\text{mod},i} - \Delta\Sigma_{\text{obs},i})^2}{\sigma_i^2} + \sum_i^n \ln(2\pi\sigma_i^2) \quad (14)$$

where the sum over i is for $n = 11$ radius bins of each $\Delta\Sigma$ profile and σ_i is the associated observational uncertainty derived using a jackknife resampling method.

6 RESULTS

6.1 Fitting our model to the data

Finally, we combine the likelihood for SMF and $\Delta\Sigma$ profiles for the model:

$$\ln \mathcal{L}_{\text{tot}} = \ln \mathcal{L}_{\text{SMF}} + \sum_j^m \ln \mathcal{L}_{\Delta\Sigma_j} \quad (15)$$

The sum over j is for the $m = 12$ aperture mass bins. To sample the posterior distributions of model parameters, we choose to use the `affine invariant MCMC ensemble sampler emcee` (Foreman-Mackey et al. 2013). We use an ensemble of 256 walkers. Following the strategy of the SED fitting code `prospector` (Johnson et al. in prep.), we separate the burn-in stage into three separated rounds, each with 150 steps. We reinitialize the walkers at the end of each round using the current best position of the ensemble and the covariance matrix measured using positions of 50 per cent walkers. This method can effectively remove stalled walkers and helps the chains to converge. After the burn-in stage, we sample another 400 steps to form the posterior distributions of parameters. Following `prospector`, we use the Kullback–Leibler divergence to check the convergence of our chains. The trace plot of this model is available here: [📄](#)

We choose weakly informative priors for the seven parameters in our model. Following the recommendation by Gelman et al. (2009), we adopt a Student- t distribution with one degree of freedom as a prior distribution for the slopes in all of the log-linear scaling relations in our model (a , c , and A_{exs}). For other parameters (b , d , f_{ins} , and B_{exs}), we choose simple top-hat distributions with reasonable boundaries. For instance, the the upper limit for *in situ* stars within inner 10 kpc is naturally 1.0. We summarise the prior distributions of all seven parameters in the upper-right table of Figure 3. Different choices of prior distributions (e.g. top-hat distributions for all parameters) does not alter key conclusions of this work.

6.2 Performance of the best-fit model

Here we summarize the key results from our best-fit model. Figure 3 presents the best-fit parameters along with their 68 per cent confidence intervals. We show the two-dimensional marginalized probability densities of these parameters and the histograms of their marginalized posterior distributions using corner plots⁸. The parameters are well-constrained. The correlations between a and b , also between A_{exs} and B_{exs} , are expected.

As shown in Figure 4, the best-fit model is capable of reproducing the observations, including the SMFs for both $\mathcal{M}_\star^{\text{Max}}$ and \mathcal{M}_\star^{10} , and the $\Delta\Sigma$ profiles in different aperture mass bins. The predicted SMFs of \mathcal{M}_\star^{10} and $\mathcal{M}_\star^{\text{Max}}$ are consistent with the observed galaxies at $\log_{10}(M_{\star,\text{max}}/M_\odot) > 11.6$ within uncertainties. And the predicted SMF of $\mathcal{M}_\star^{\text{Max}}$ is also consistent with the SMF from the PRIMUS survey at similar redshift range (Moustakas et al. 2013) down to $\log_{10}(M_{\star,\text{max}}/M_\odot) \sim 11.2$ where no observations are included. As for the $\Delta\Sigma$ profiles, the overall goodness-of-fit is excellent, although small mismatches can be found at > 1 Mpc in a few aperture mass bins (e.g. bin 1, 2, & 12).

6.3 Best fit TSMR and SHMR

6.3.1 TSHMR

From the best-fit model, we have the TSHMR:

$$\log \mathcal{M}_\star^{\text{all}} = 0.602_{-0.006}^{+0.005} \times (\log M_{\text{vir}} - 13.5) + 11.846_{-0.003}^{+0.003} \quad (16)$$

We show the distribution of central galaxies on the $M_{\text{vir}} - M_\star^{\text{all}}$ plane and the median TSHMR in panel (a) of Figure 5. The best-fit SHMR is indeed very tight. In fact, as indicated by the best-fit c and d , the TSHMR has very little scatter. As explained earlier, this scatter is supposed to account for both intrinsic scatter and measurement uncertainties. Hence such small scatter is unlikely to be realistic. In Appendix A, we show that the current `UniverseMachine` model has a large scatter of δ_{gal} for central galaxies at fixed M_\star^{all} . It seems such scatter alone can account for the intrinsic scatter of SHMR and uncertainties of stellar mass measurements when comparing to observations, practically leaving no room for additional scatter of the TSHMR. Although previous works have also commented on the apparent tightness of the TSHMR (e.g. van der Burg et al. 2014; Patel et al. 2015; Kravtsov et al. 2018), it remains an open question whether TSHMR scatter is genuinely as tight as indicated by these and our results.

Figure 6 compares the best-fit TSHMR with other observational constraints of groups and clusters at similar redshifts. Leauthaud et al. (2012b) constrain the TSHMR of groups in the COSMOS field at $0.22 < z < 0.48$. Budzynski et al. (2014) derive the TSHMR for a large sample of low-redshift SDSS groups and clusters using optical richness. Patel et al. (2015) estimate the TSHMR for X-ray groups ($M_{200c} < 10^{13.5} M_\odot$) in the *Chandra* Deep Field South (CDF-S) field. And Kravtsov et al. (2018) measure the TSHMR for 21 massive $z \sim 0$ clusters using X-ray observations and improved photometric models of massive brightest cluster

⁸ The corner plot is generated by `corner.py`

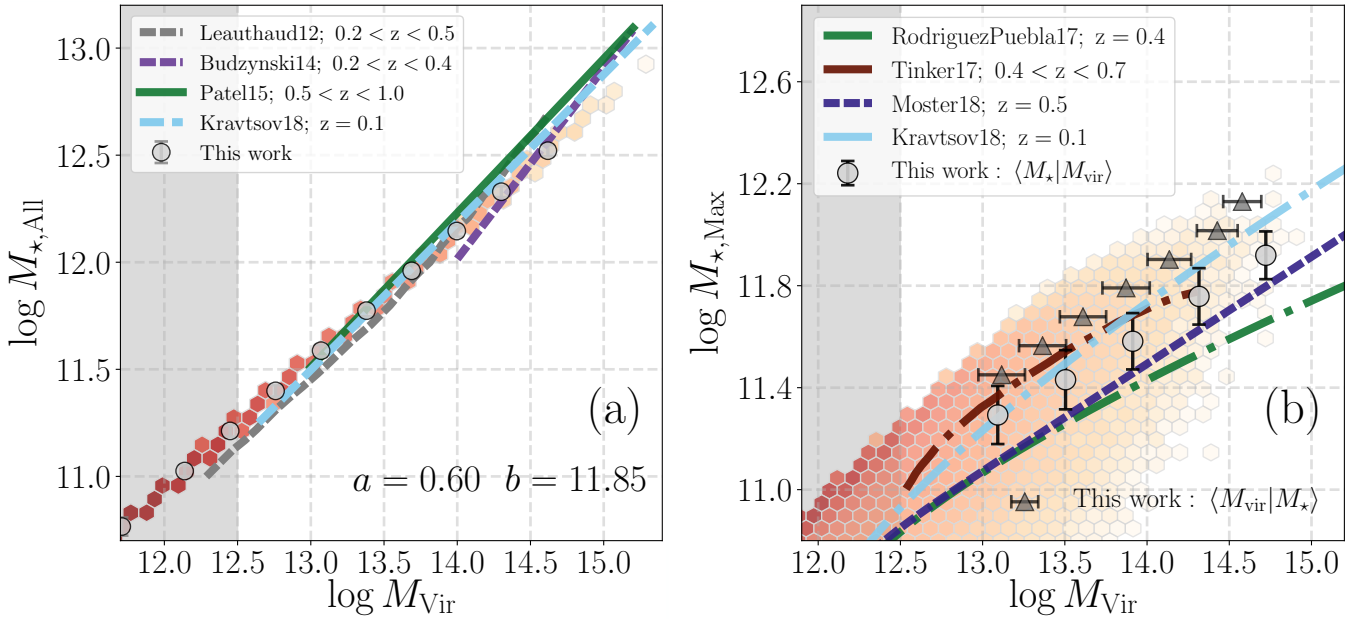


Figure 5. (a) Comparison between the TSHMR from our model and other work. The background density plots show the distributions of modelled galaxies where the color indicates the number density of galaxies. TSHMR from literature includes Leauthaud et al. 2012b (dashed grey line), Budzynski et al. 2014 (dashed purple line), Patel et al. 2015 (solid green line), and Kravtsov et al. 2018 (dashed teal line). Our median TSHMR is highlighted by grey circles. (b) Comparison between the SHMR of central galaxies from our best-fit model and recently published SHMRs at similar redshifts, including Rodríguez-Puebla et al. 2017 (dot-dashed green line), Tinker et al. 2017 (dot-dashed brown line), Moster et al. 2018 (dashed purple line), Kravtsov et al. 2018 (solid pink line). For the median SHMR: the grey circles show the median M_{\star}^{max} at different M_{\star}^{max} bins while the grey triangles show the median M_{Vir} at fixed M_{\star}^{max} . Error bars indicate the scatter of M_{\star}^{max} or M_{Vir} within the bin. All comparisons are under the same fiducial assumptions of h -factor $h = 0.7$, Chabrier IMF, and FSPS stellar population models. The Jupyter notebook for this figure is available here: [📄](#)

galaxies (BCGs). The slope of our TSHMR (0.602 ± 0.005) is shallower than some previous estimates (e.g. 0.89 ± 0.14 in Budzynski et al. 2014; 0.84 ± 0.10 in Patel et al. 2015; also see Giodini et al. 2009; Lin et al. 2012), but once we convert different TSHMRs into $h = 0.7$ with the Chabrier IMF, the overall agreement is good.

Our TSHMR is constrained by the deepest imaging dataset for a large sample of massive galaxies and high signal-to-noise g - g lensing measurements. The best-fit relation is consistent with other observational constraint down to $\log_{10} M_{\text{Vir}} \geq 12.5$, which extends below the halo mass range probed by the observed massive galaxies. This further suggests that the total stellar mass in a dark matter halo is an excellent proxy of halo mass (although see discussion about the scatter of the TSHMR.).

6.3.2 SHMR

Figure 6 displays the number density distribution of model galaxies (indicated by color) over the $M_{\text{Vir}}-M_{\star}^{\text{max}}$ plane. As discussed in Tinker et al. (2017) and Rodríguez-Puebla et al. (2017), the non-Gaussian distribution of galaxies along the SHMR causes differences between SHMR when described by the mean M_{\star}^{max} at fixed M_{Vir} ($\langle M_{\star} \rangle_{M_{\text{Vir}}}$; grey circles) and by the mean M_{Vir} in bins of M_{\star}^{max} ($\langle M_{\text{Vir}} \rangle_{M_{\star}^{\text{max}}}$; grey triangles).

A log-linear fit for $\langle M_{\star} \rangle_{M_{\text{Vir}}}$ at $\log M_{\text{Vir}} \geq 13.0$ yields:

$$\log M_{\star}^{\text{max}} = 0.36 \pm 0.01 \times (\log M_{\text{Vir}} - 13.27) + 11.38 \pm 0.02 \quad (17)$$

with a scatter of $\sigma_{\log M_{\text{Vir}}} = 0.23 \pm 0.01$. The best-fit log-linear relation for $\langle M_{\text{Vir}} \rangle_{M_{\star}^{\text{max}}}$ at $\log M_{\star}^{\text{max}} \geq 11.5$ is:

$$\log M_{\text{Vir}} = 2.49 \pm 0.02 \times (\log M_{\star}^{\text{max}} - 11.6) + 13.39 \pm 0.02 \quad (18)$$

with a scatter of $\sigma_{\log M_{\star}^{\text{max}}} = 0.22 \pm 0.01$.

We compare our results with recent constraints of SHMR in the form of $\langle M_{\star} \rangle_{M_{\text{Vir}}}$ ⁹. Tinker et al. (2017) estimate the SHMR for massive ($\log M_{\star} \geq 11.4$) CMASS galaxies (e.g. Dawson et al. 2013) at $0.4 < z < 0.7$ using clustering measurements. The SHMR from Kravtsov et al. (2018) show here is from an abundance matching method based on the SMFs from Bernardi et al. (2013). The SHMRs of Rodríguez-Puebla et al. (2017) and Moster et al. (2018) are from two new semi-empirical models that are similar to the UniverseMachine in methodology.

Recent empirical models (e.g. Rodríguez-Puebla et al. 2017; Moster et al. 2018; Behroozi et al. 2018) have adopted the improved $z \sim 0$ SMF from Bernardi et al. (2013) which uses a better background subtraction. This approach could lead to better agreement with our result using deep HSC images than earlier models that are constrained by local SMFs that underestimate the masses of massive galaxies (e.g. Behroozi et al. 2013b).

Scatter in the SHMR includes an intrinsic component

⁹ All SHMR have also been converted to $h = 0.7$, Virial halo mass and the Chabrier IMF.

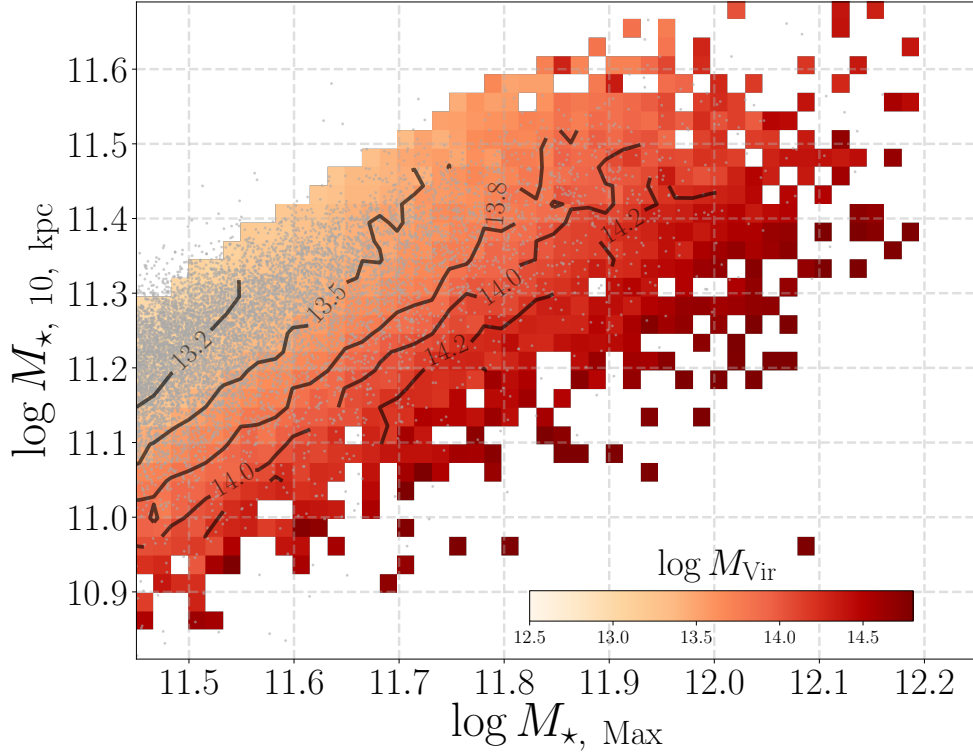


Figure 6. Variation of halo mass across the aperture mass plane based on the best-fit ASAP model for massive central galaxies. Grey points in the background show the distribution of HSC galaxies. Color of the density plot labels the average M_{vir} from the model. Black contours highlight ‘iso- M_{vir} ’ curves over this 2-D plane. The Jupyter notebook for this figure is available here: [🔗](#)

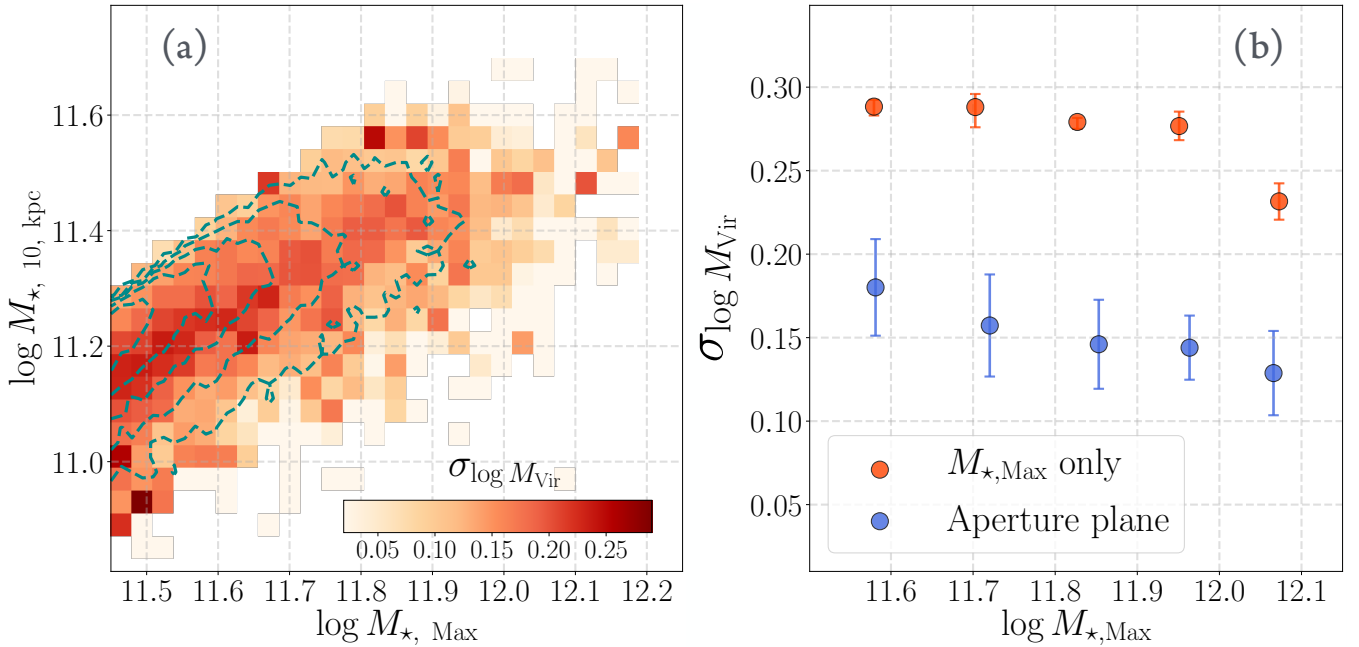


Figure 7. (a) Scatter of $\log_{10} M_{\text{vir}}$ across the aperture mass plane. The distribution of HSC galaxies is outlined using contours (grey dashed-line). (b) Scatter of $\log_{10} M_{\text{vir}}$ at different M_{\star}^{max} . Red points correspond to the scatter in different M_{\star}^{max} bins. Blue points show the mean scatter when information from the aperture mass plane is considered. The errors bars are estimated by randomly drawing from the posterior distributions of model parameters. Scatter here includes both an intrinsic component as well as the uncertainty of stellar mass measurements. The Jupyter notebook for this figure is available here: [🔗](#)

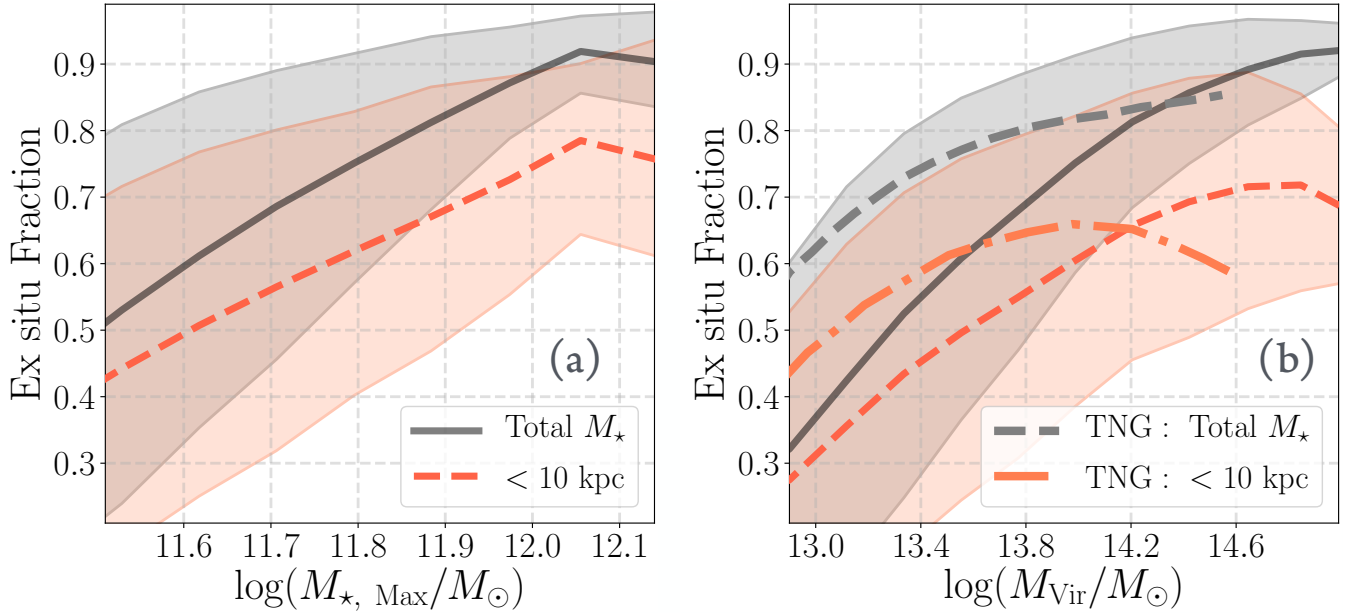


Figure 8. (a) The relation between the fraction of *ex situ* stars and stellar mass (M_{\star}^{\max}) using the best-fit ASAP model. (b) The same relation between halo mass (M_{vir}). Solid black lines and the corresponding shaded regions are for the *ex situ* fraction in the total stellar mass, while the dashed-red lines and the associated shaded regions indicate the *ex situ* fraction within 10 kpc. The shaded regions describe the 1σ uncertainties. In massive galaxies, *ex situ* stars dominate the total stellar mass budget and the central stellar mass when $\log_{10}(M_{\star, \text{max}}/M_{\odot}) > 11.5$ or when $\log_{10} M_{\text{vir}} > 13.5$. In (b) we also compare our results with similar relations from the TNG300 simulation (see Pillepich et al. 2018a for details). The *Jupyter* notebook for this figure is available here: [📄](#)

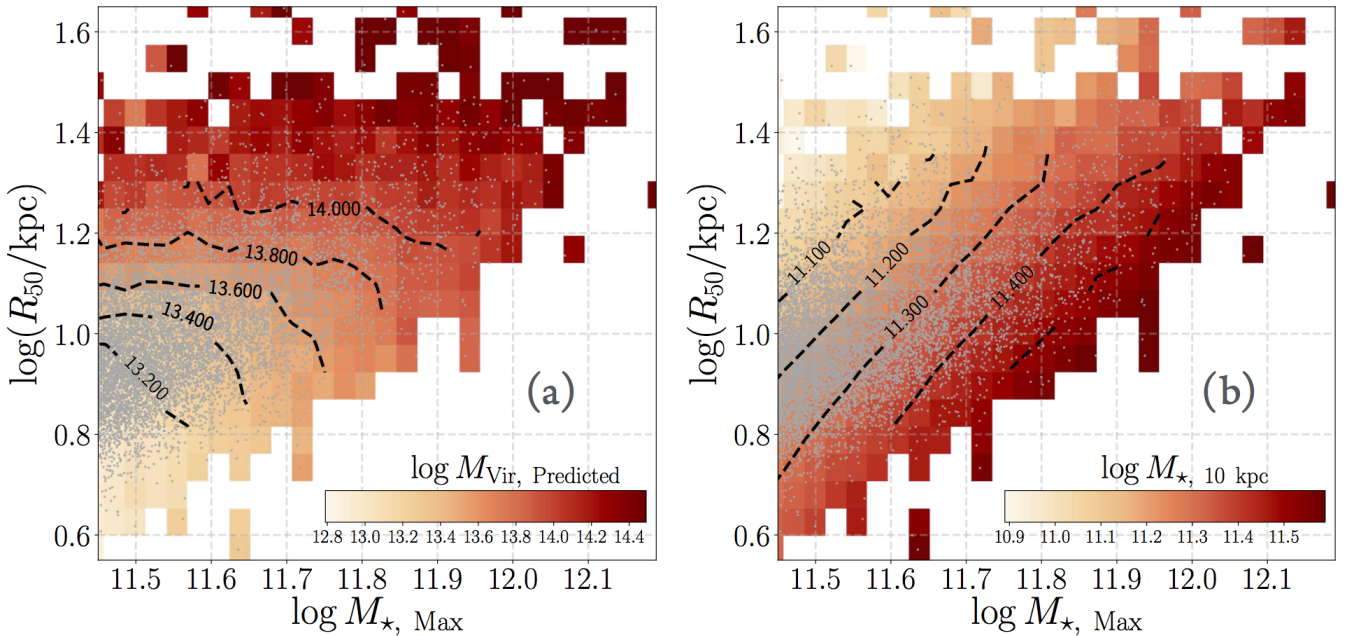


Figure 9. Stellar mass (M_{\star}^{\max})–galaxy size (R_{50}) relation color-coded by the predicted halo mass (M_{vir}) from the best-fit model (a) and the stellar mass within 10 kpc (b). For each HSC galaxy, we assign a M_{vir} using the best-fit M_{\star}^{\max} – M_{\star}^{10} – M_{vir} relation. The *Jupyter* notebook for this figure is available here: [📄](#)

and uncertainties of stellar mass measurements. Our results agree well with recent constraints when described by $\sigma_{\log M_\star}$ at fixed M_{vir} . Tinker et al. (2017) find $\sigma_{\log M_\star} = 0.18^{+0.01}_{-0.02}$ at $\log M_\star \geq 11.4$. The *Emerge* model by Moster et al. (2018) shows a scatter of $\sigma_{\log M_\star} = 0.16$ at high masses. Along with other recent work (e.g. Reddick et al. 2013; Zu & Mandelbaum 2016), these estimates leave little room for intrinsic scatter in the high mass SHMR ($\sigma_{\log M_\star}^{\text{intr}} < 0.16$).

In our model, the scatter in the SHMR is a result of the TSHMR and the scatter in $f_\star^{\text{cen}} = M_\star^{\text{cen}}/M_\star^{\text{all}}$ as predicted by the *UniverseMachine* model. Physically, the decreasing scatter of f_\star^{cen} may result from the central limit theorem during the complex merging history of massive haloes (e.g. Gu et al. 2016). This scatter is discussed in further detail in the following section.

6.4 Variations of M_{vir} across the $M_\star^{\text{max}}-M_\star^{10}$ plane

The main goal of our model is to evaluate the $M_\star^{\text{max}}-M_\star^{10}-M_{\text{vir}}$ relation. Figure 6 displays variations in M_{vir} across the aperture mass plane. This trend is strongly constrained by the $\Delta\Sigma$ profiles in different aperture mass bins. The variation is also consistent with the intuition we initially gained from Figure 4. The amplitude of $\Delta\Sigma$ increases with M_\star^{max} but also decreases with M_\star^{10} at fixed M_\star^{max} . This indicates higher M_{vir} for massive galaxies with more extended stellar envelopes.

The median M_{vir} in each bin is shown on the upper-right corner of each panel. Typically, the range of M_{vir} across the three bins with similar M_\star^{max} is about 0.15-0.20 dex. But, as shown in panel (a) of Figure 4, this is caused by the choices of M_\star^{10} bins at fixed M_\star^{max} : although they cover very different ranges of M_\star^{10} , the mean M_\star^{10} values for the three bins are not very different due to the distribution of massive galaxies. Right now the choice of mass bins is limited by the required number of galaxies to ensure sufficient S/N of the $\Delta\Sigma$ profile and uncertainties of stellar mass measurements (~ 0.1 dex). This is not ideal for direct measurement of ‘local’ M_{vir} across the aperture mass plane and is precisely why we choose to use the forward modelling approach by simultaneously considering twelve $\Delta\Sigma$ profiles and two SMFs so that we can still use the best-fit model to explore the M_{vir} trend in more detail.

The iso- M_{vir} curves on Figure 7 run almost parallel to the $M_\star^{\text{max}}-M_\star^{10}$ relation, resulting in a considerable range of M_{vir} (> 0.7 dex) in the vertical direction at fixed M_\star^{max} . This range is not surprising, however, given the range of M_{vir} seen on the SHMR at fixed M_\star^{max} (e.g. see Figure 5; also see Figure 9 in Tinker et al. (2017)). What is surprising, however, and this is one of the main results of this paper, is that a large fraction of the scatter can be accounted for by structural variations in massive galaxies. In other terms, the scatter in M_{vir} is greatly reduced in the aperture mass plane compared to the SHMR. Figure 7 displays the scatter of M_{vir} ($\sigma_{\log M_{\text{vir}}}$) across the aperture mass plane. Among regions occupied by most massive galaxies (indicated by the contours), the typical scatter is only of order 0.15 dex.

Figure 7 suggests that the combination of $M_\star^{\text{max}}-M_\star^{10}$ predicts M_{vir} better than M_\star^{max} alone. For instance, a simple

random forest regressor¹⁰ can provide an accurate description of the $M_\star^{\text{max}}-M_\star^{10}-M_{\text{vir}}$ 3-D space and can be used to predict M_{vir} (see Appendix B). However, with random forest there is a risk of overfitting, and the results are not intuitive. We therefore also fit the $M_\star^{\text{max}}-M_\star^{10}-M_{\text{vir}}$ plane using the robust linear regression algorithm *LtsFit* (Cappellari 2014). The best-fit relation is:

$$\log M_{\text{vir}} = 3.26 \pm 0.02 \times (\log M_\star^{\text{max}} - 11.72) - 2.46 \pm 0.03 \times (\log M_\star^{10} - 11.34) + 13.69 \pm 0.01 \quad (19)$$

with a scatter of $\sigma_{\log M_{\text{vir}}} = 0.16 \pm 0.01$. As shown in Appendix B, this simple relation is also capable of predicting M_{vir} with reasonable precision and a smaller scatter than the SHMR. We further discuss predictive capabilities in Section 7.2.

6.5 *In situ* and *ex situ* fractions

Since the version of *UniverseMachine* used here predicts the M_\star of the *in situ* and *ex situ* components, our model can be used to shed light on the statistical behaviors of these two components. The best-fit model suggests that 67 ± 1 per cent of *in situ* stars can be found within 10 kpc, while the fraction of *ex situ* stars within 10 kpc slowly decreases with M_{vir} due to the increasingly extended distribution of the *ex situ* component. At $M_{\text{vir}} = 10^{13} M_\odot$, about half of the *ex situ* stars lie inside 10 kpc according to the best-fit model. This fraction decreases to ~ 30 per cent for a $M_{\text{vir}} = 10^{14} M_\odot$ halo.

Focusing on the *ex situ* component, we show how the fraction of *ex situ* stars changes with M_\star^{max} and M_{vir} in Figure 8. In agreement with results from recent hydro-simulations (e.g. Rodriguez-Gomez et al. 2016; Qu et al. 2017; Pillepich et al. 2018b), the *ex situ* fraction increases with both stellar and halo mass, and it remains the dominant stellar component in massive galaxies. Remarkably, this is not just the case for the galaxy as a whole, but it is even true on 10 kpc scale for these massive galaxies. For central galaxies with $\log_{10}(M_{\star, \text{max}}/M_\odot) > 11.5$ and in haloes with $\log_{10} M_{\text{vir}} > 13.5$, the average *ex situ* fraction at $r < 10$ kpc is > 50 per cent.

In Figure 8, we also compare the trends of the *ex situ* fraction with halo mass with results from the *IllustrisTNG* simulation (Pillepich et al. 2018b; TNG hereafter). We find reasonable qualitative agreement between our model and the TNG simulation; differences in detail are to be expected, given the different methods used for measuring M_\star (Ardilla et al in prep), e.g., for the *ex situ* fraction within 10 kpc, Pillepich et al. (2018b) use a 3-D sphere while we use a 2-D elliptical aperture.

The dominant role of *ex situ* stars at the centers of massive galaxies has been discussed by Cooper et al. (2013) using a particle-tagging method and by Rodriguez-Gomez et al. 2016 using the *Illustris* simulation. It is likely that these *ex situ* stars originate from major mergers that happened at

¹⁰ e.g. The *RandomForestRegressor* from *scikit-learn* package. Random forest is a flexible machine learning algorithm that uses a combinations of multiple decision trees to make predictions based on the data.

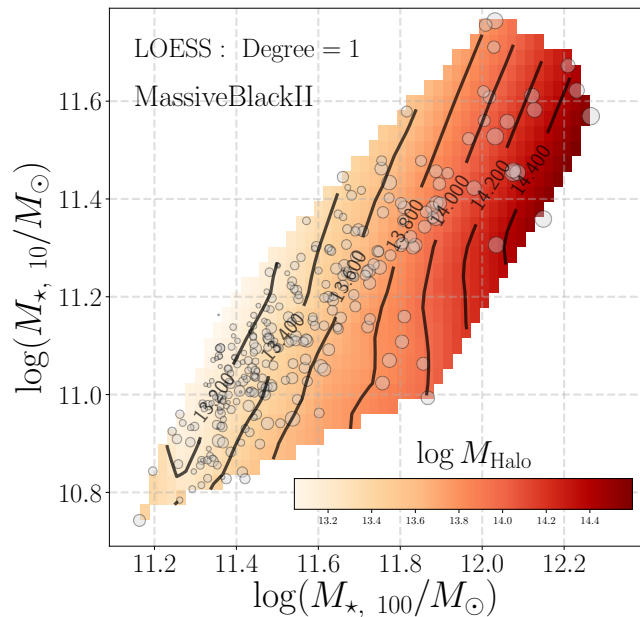


Figure 10. The M_{\star}^{100} and M_{\star}^{10} of massive galaxies from the **MassiveBlackII** simulation using randomly projected 2-D stellar mass distributions. The plot shows their distributions over the aperture mass plane color-coded by halo mass. The density plot shows the halo mass trend recovered by the LOESS smoothing method. The **Jupyter** notebook for this figure is available here: [🔗](#)

high- z . This is directly related to the current definition of the *in situ* and *ex situ* components. We discuss this further in Section 7.3.

6.6 Relation between M_{vir} and galaxy size

Figure 9 shows variations in the mean M_{vir} across the mass-size relation. Here we use M_{\star}^{max} and a non-circulized half-light radius measured using a 1-D stellar mass curve of growth. For each massive galaxy, we assign a M_{vir} using the best-fit $M_{\star}^{\text{max}}-M_{\star}^{10}-M_{\text{vir}}$ relation derived above. We do not attempt to remove satellite galaxies.

In **Paper I**, we showed that massive central galaxies in halos of different mass exhibit a distinct mass-size relation. Panel (b) of Figure 9 presents more sophisticated constraints on this ‘environmental’ dependence of mass-size relation: M_{vir} varies systematically across this plane, and the iso- M_{vir} curves here are almost perpendicular to the mass-size relation. *At fixed M_{\star}^{max} , galaxies with larger size tend to live in more massive haloes.* This suggests that the sizes of massive galaxies also carry clues about their dark matter halo mass, as discussed in **Kravtsov (2013)**. However, as discussed in **Paper I**, the measurement of ‘galaxy size’ often depends on the assumed photometric model and data quality. Therefore, we prefer to build our empirical model based on a more straightforward aperture mass plane instead of the mass-size relation.

7 DISCUSSION

7.1 Comparison with hydrodynamic simulations

From HSC $g-g$ lensing measurement and our best-fit model, we find that the halo masses of massive galaxies vary systematically across the aperture mass plane. This reveals a clear connection between the distribution of stars within massive galaxies, and halo mass. We now investigate if such correlations are also predicted by hydrodynamic simulations of galaxy evolution.

We compare the observed $M_{\star}^{\text{max}}-M_{\star}^{10}-M_{\text{vir}}$ relation with the relations of massive galaxies from the **MassiveBlackII** simulation (e.g. **Khandai et al. 2015**; **Tenneti et al. 2015**). **MassiveBlackII** is a state-of-the-art, large-volume ($100h^{-1}$ Mpc box size; 1792^3 gas particles), high-resolution cosmological simulation using **p-Gadget** (**Springel 2005**). It includes a sophisticated treatment of complex baryonic physics (e.g. star formation in a multiphase interstellar medium, black hole accretion and feedback, and radiative cooling and heating processes). For additional information about the physical details and general performance of the **MassiveBlackII** simulation, please refer to **Khandai et al. (2015)**.

We select 291 massive galaxies with $\log(M_{\star}/M_{\odot}) \geq 11.4$ from the **MassiveBlackII** simulation and generate randomly projected 2-D stellar mass maps with a 2 kpc pixel resolution and 350 kpc image size. Then we treat them as real data and measure their aperture masses using the same method for HSC massive galaxies (**Ardila et al. in prep.**). We choose to use 10 and 100 kpc elliptical apertures here. In Figure 10, we show the trend of halo mass across this aperture mass plane recovered by the locally weighted regression (LOESS) method (**Cleveland & Devlin 1988**; **Cappellari et al. 2013**)¹¹. The trend is qualitatively similar to our results, while the slope of the iso- M_{vir} curves appears to be steeper than those of our best-fit model.

Currently, comparison with simulation is limited by the volume of high-resolution hydro-simulations and their capabilities to reproduce realistic massive galaxies. The SMF of massive galaxies using M_{\star}^{100} and the stellar mass density profiles of massive galaxies **MassiveBlackII** do show differences compared with the HSC observations (see **Ardila et al. in prep.**). Nonetheless, we consider this to be a valuable test and we will further investigate the robustness of this trend using other hydro simulations in future work.

7.2 Prediction of halo mass

Our **ASAP** model suggests that, by including information about the stellar mass distribution (e.g. two-aperture stellar masses), one can build better proxies of halo mass. We test this potential by predicting the halo masses of massive clusters from the **Cluster Lensing And Supernova survey with Hubble** (CLASH) clusters (e.g. **Postman et al. 2012**) using only the photometry of their brightest cluster galaxies.

DeMaio et al. (2018) conducted a careful study of the BCG+ICL of 23 CLASH clusters ($0.3 < z < 0.9$; $3 \times 10^{13} < M_{500c}/M_{\odot} < 9 \times 10^{14}$) using multiband, high-resolution HST

¹¹ We use the Python implementation of **2-D LOESS** by Michelle Cappellari.

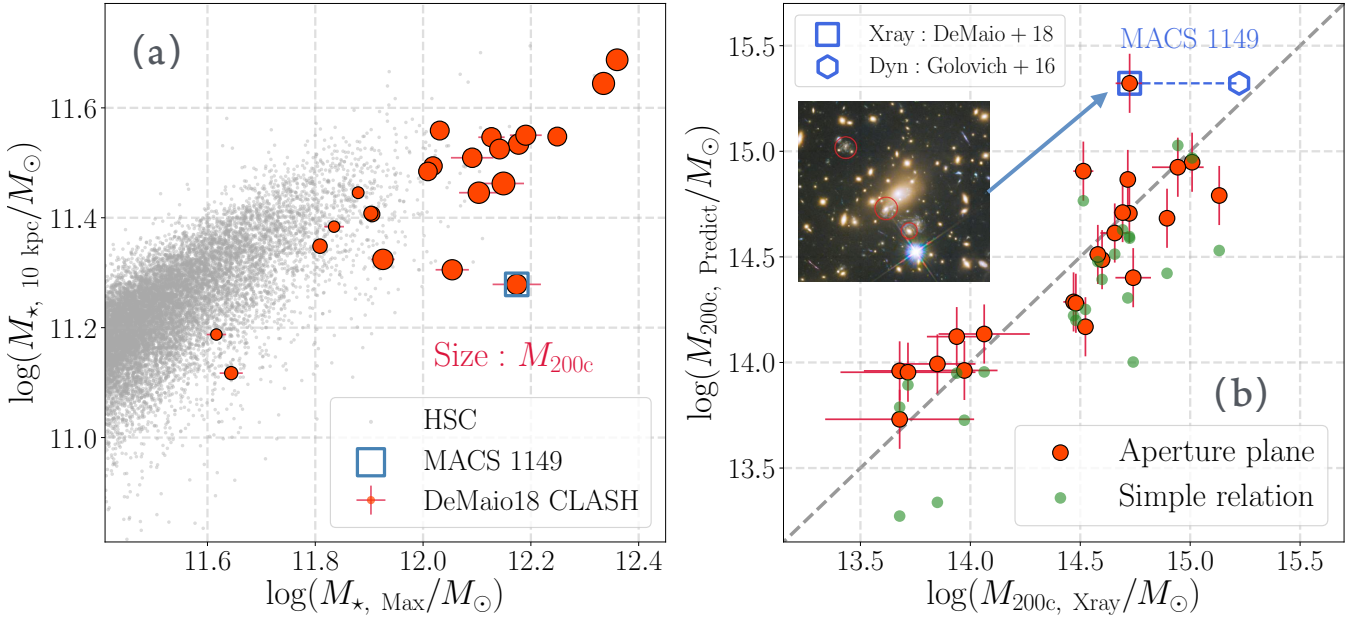


Figure 11. (a) Distribution of CLASH BCGs in the aperture mass plane. The stellar masses are based on Hubble Space Telescope (HST) observations (DeMaio et al. 2018; red points), where the symbol size indicates halo mass (M_{200c}) estimated from X-ray observations. (b) Comparison between our predicted M_{200c} values to those based on X-ray observations. Green points are predictions based on the $M_{\star}^{\text{max}}-M_{\text{vir}}$ relation, whereas red points are based on the best-fit aperture mass plane. The dashed line shows the one-to-one relation. The prediction using the aperture mass plane shows a tighter relation compared to X-ray masses. The outlier system, MACS1149, is highlighted using a blue box. We also show the colored HST image of the BCG of MACS1149. The blue hexagon shows the value of M_{200c} as measured via dynamics (Golovich et al. 2016). The Jupyter notebook for this figure is available here: [📄](#)

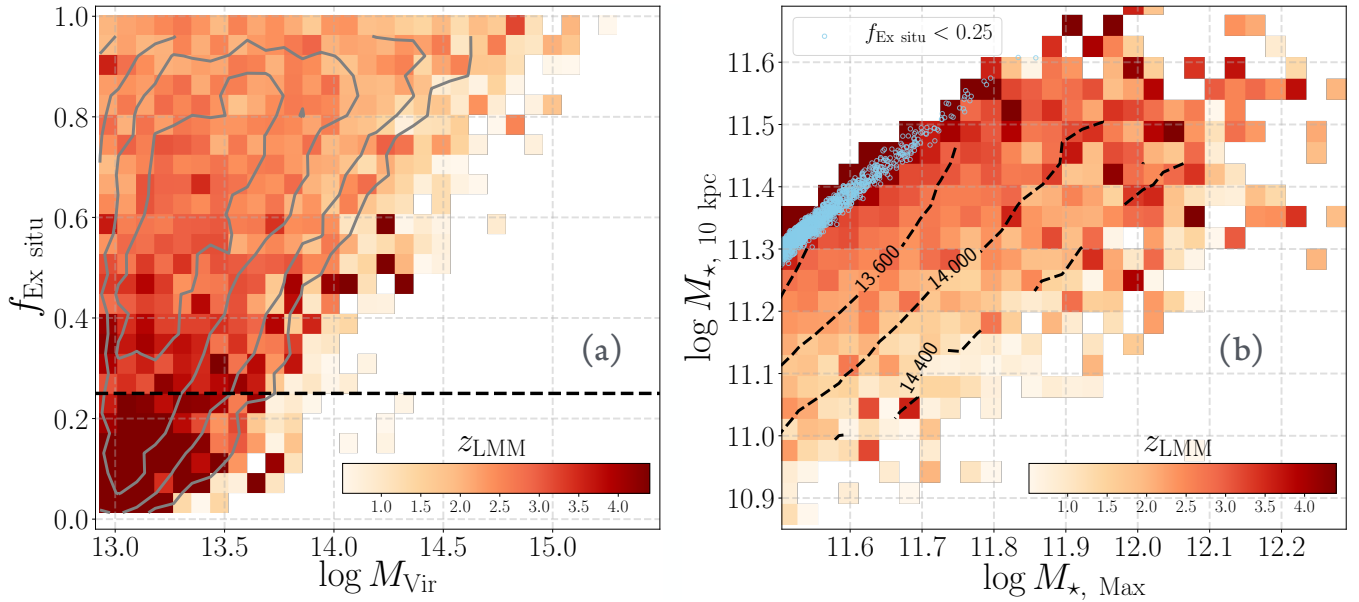


Figure 12. (a) Relation between the halo mass (M_{vir}) and the fraction of *ex situ* stars for massive galaxies ($\log_{10}(M_{\star, \text{max}}/M_{\odot}) \geq 11.5$) color-coded by the redshift of last major-merger (z_{LMM} ; halo mass ratio larger than 1:3) in the UniverseMachine model. The grey contours outline the number density distribution of model galaxies. A horizontal dashed line highlights the 25 per cent limit that is used to define massive galaxies with low *ex situ* fraction. (b) The aperture mass plane for massive galaxies from the best-fit model color-coded by z_{LMM} . Grey contours here indicate the iso- M_{vir} lines. The small population of massive model galaxies with $f_{\text{Ex situ}} < 0.25$ is highlighted with light-blue dots. The Jupyter notebook for this figure is available here: [📄](#)

Wide Field Camera 3 (WFC3) images. These authors derive surface brightness and color profiles of these BCG+ICL to $r > 100$ kpc, along with stellar mass within 10 and 100 *circular* apertures using SED fitting. We ignore the differences caused by circular and elliptical apertures here and increase their 100 kpc aperture mass by +0.05 dex to simulate our M_{\star}^{\max} measurement (see Paper I). After converting their aperture masses to the same cosmology and stellar population model¹² used here, we predict the M_{vir} of these BCGs using our best-fit model. The CLASH sample includes mostly very massive clusters that host BCGs that are on average more massive than the HSC sample (panel (a) of Figure 11).

Figure 11 shows halo masses predicted both by the average M_{\star}^{\max} - M_{vir} relation shown in Figure 5 (green dots) and by the best-fit M_{\star}^{\max} - M_{\star}^{10} - M_{vir} relation (red circle). In DeMaio et al. (2018), halo mass is measured using X-ray observations (e.g. Vikhlinin et al. 2009) and is defined as M_{500c} . Using empirical relations from (Diemer et al. 2013; Diemer & Kravtsov 2015) and the Colossus Python package (Diemer 2017; code available here: <https://github.com/colossus-python/colossus>), we convert both the M_{500c} in DeMaio et al. (2018) and the M_{vir} from our model to M_{200c} . It is encouraging to see that the predicted halo mass values show good consistency with those based on X-rays. The values predicted using M_{\star}^{\max} alone show larger scatter compared to the X-ray mass estimates. This provides further evidence for one of the key findings of the present work: two-aperture stellar masses can be used to build better proxies of halo mass relative to models using M_{\star}^{\max} alone.

There is one BCG that shows a large offset (highlighted in both panels of Figure 11) from the mean relations. The BCG belongs to the famous cluster MACS 1149+22 at $z = 0.544$ (see the inset picture) that gifted us multiple images of a highly magnified supernova (e.g. Kelly et al. 2015) and a $z \sim 9.1$ galaxy (e.g. Hashimoto et al. 2018). The region around the BCG is complex and partially overlaps with an image of a background star-forming galaxy. We suspect that the accuracy of photometry and M_{\star}/L_{\star} estimation are affected by the complexity of extracting photometry for this system. Moreover, it is possible that the X-ray gas underestimates the halo mass due to non-thermal pressure support or projection effect (e.g. Evrard 1990; Nagai et al. 2007; Mahdavi et al. 2008). Golovich et al. (2016) estimate the halo mass of MACS 1149+22 using dynamics of cluster members. The dynamics-based M_{200c} is higher than the X-ray value and is closer to our prediction.

At the same time, we acknowledge that different methods sometimes lead to systematically different measurements of M_{200c} . For example, it is known that M_{200c} calibrated using weak lensing is often larger compared to X-ray based masses for massive clusters (e.g. Simet et al. 2017). Indeed, weak lensing measurements of some massive CLASH clusters in DeMaio et al. (2018) result in noticeably more massive M_{200c} than those derived from X-ray's (see Umetsu et al. 2014). These types of offsets are beyond the scope of this work, but are worth investigating in the future to further

improve our predictions of halo mass using aperture stellar masses.

7.3 The fraction of *ex situ* stars in massive galaxies

Figure 8 shows that the *ex situ* fraction predicted by our model and its relation with both stellar and halo mass are reasonable and are qualitatively consistent with hydro-simulation (e.g. TNG300). We now discuss two points in Figure 8 of noteworthy interest.

First, the large scatter in *ex situ* fractions at fixed stellar or halo mass suggests a small population of massive galaxies with low *ex situ* fractions (< 25 per cent). This special population could experience fewer mergers (especially major mergers) and is an interesting sample to study in greater detail.

On panel (a) in Figure 12, we color-code the $M_{\text{vir}}-f_{\text{ex}}$ relation for massive galaxies ($\log_{10}(M_{\star, \text{max}}/M_{\odot}) \geq 11.5$) in our best-fit model using the redshift of the last major halo merger (halo mass ratio larger than 1:3) extracted from the merger trees of SMDPL haloes. We find that massive galaxies with low *ex situ* fraction tend to live in relatively low mass haloes and have not experienced major-mergers in the last 10 Gyrs, putting them among the oldest massive haloes in the universe. This small (~ 9 per cent of massive galaxies with $11.5 < \log_{10}(M_{\star, \text{max}}/M_{\odot}) \leq 11.7$) population locates exclusively on the upper-edge of the aperture mass plane (panel (b) of Figure 12). Such a special location suggests that they are much more compact than the similarly massive ones with a richer merging history. If haloes with such a unique assembly history are not artifacts of the UniverseMachine model, they could be very useful for studying galaxy assembly bias (e.g. Cooper et al. 2010; Wang et al. 2013; Zentner et al. 2014; Lin et al. 2016) or for providing a template of the distribution of *in situ* stars in massive haloes. The galaxies discussed here would be somewhat different in nature than ‘relic’ galaxies¹³ (e.g. Trujillo et al. 2014; Peralta de Arriba et al. 2016; Yıldırım et al. 2017; Ferré-Mateu et al. 2017): the population under discussed here are more massive than typical relic galaxies, are larger in size, and are unaffected by stripping as this sample is predominantly centrals.

Second, both the ASAP model and hydro-simulations predict a high *ex situ* fraction in the inner regions of massive galaxies. This is easy to understand given the current definition of *ex situ* stars. This is commonly defined as all the stars that are formed outside the halo of the *main progenitor*. The *ex situ* component therefore includes stars that were accreted from major mergers at very high redshift (e.g. $z > 2$). Although this is a straightforward definition, it may not be the best choice to relate to observational studies of the stellar assembly history of massive galaxies for two reasons. First, it makes the *ex situ* component heterogeneous since *ex situ* stars can be formed at very different epochs and in haloes with a wide range of M_{vir} . Second, it is hard to separate the *in situ* and *ex situ* stars in the inner regions of massive

¹² DeMaio et al. (2018) uses the BC03 stellar population model. Based on tests from Paper I, we add a +0.1-dex empirical correction to the Flexible Stellar Population Synthesis (FSPS) mode used in this work.

¹³ Typically defined as nearby compact quiescent galaxies with stellar mass and effective radius similar to the quiescent galaxies at high-redshift.

galaxies because stars in both components are assembled at a very early time and share similar stellar population and kinematic properties. Although it is beyond the scope of this work, we argue that it may be worth considering alternative and potentially more instructive decompositions for massive galaxies.

8 SUMMARY AND CONCLUSIONS

Using data from the HSC survey, we perform careful aperture mass and weak lensing measurements for a sample of $\sim 3200 \log_{10}(M_{\star, \text{max}}/M_{\odot}) > 11.6$ super massive galaxies. Using weak lensing, we reveal a tight connection between the stellar mass distribution of super massive central galaxies and their total dark matter halo mass. *At fixed ‘total’ stellar mass (M_{\star}^{max}), massive galaxies with more extended mass distributions tend to live in more massive dark matter haloes.* This provides a new and independent confirmation, backed by direct weak lensing measurements, of the results from [Paper II](#) that M_{vir} varies systematically over the aperture M_{\star} plane.

To model both the weak lensing and the aperture stellar mass functions, we build a full forward model based on a special version of the semi-empirical model `UniverseMachine` and the SMDPL simulation. `UniverseMachine` leverages the ability of high-resolution simulations to identify and track the full merger history of dark matter halos; using `UniverseMachine` as the bedrock of our model allows us to study the co-evolution of massive galaxies and their halos. We augment the baseline `UniverseMachine` model with two prescriptions that allow us to fit HSC data and predict aperture masses. Our model make the two following assumptions. We assume (1) a tight correlation between halo mass and the mass of its entire stellar content (TSHMR) and (2) a certain fraction of the *in situ* and *ex situ* stars locate within the inner 10 kpc of massive galaxies. In our model, the well-studied SHMR and its scatter emerge from the TSHMR. We show that this model provides an excellent description of the observed SMFs for M_{\star}^{max} and M_{\star}^{10} , as well as the $\Delta\Sigma$ profiles in a series of $M_{\star}^{\text{max}}-M_{\star}^{10}$ bins.

The main conclusions from the current best-fit model include the following:

- M_{vir} varies systematically over the aperture mass plane. The iso- M_{200b} curves run almost parallel with the direction of the $M_{\star}^{\text{max}}-M_{\star}^{10}$ relation. The model confirms that at fixed M_{\star}^{max} , galaxies with more extended stellar mass distributions (lower M_{\star}^{10} or larger size) live in more massive dark matter haloes. It also shows that scatter in M_{vir} at either fixed M_{\star}^{max} or M_{\star}^{10} is quite large.
- The above trends can be summarized into a simple $M_{\star}^{\text{max}}-M_{\star}^{10}-M_{\text{vir}}$ relation that provides a tighter connection with halo mass than M_{\star}^{max} alone.
- The usage of two aperture masses can help reduce the scatter in halo mass at fixed total stellar mass. While the standard SHMR in the form of $\langle M_{\text{vir}} \rangle_{M_{\star}}$ typically shows scatter in halo mass of ~ 0.25 dex at $11.5 < \log M_{\star}^{\text{max}}$, this scatter can be reduced to the ~ 0.15 dex level by utilizing our results based on $M_{\star}^{\text{max}}-M_{\star}^{10}-M_{\text{vir}}$ scaling relation.
- Our model predicts that the *ex situ* fraction increases with both the stellar and halo mass; and it shows that the *ex*

situ component even dominates the inner 10 kpc of massive galaxies. These predictions are consistent with results from the TNG simulations.

Our results strongly suggest that information about the assembly history of massive dark matter haloes is encoded in the stellar mass distributions of their massive central galaxies. This opens a new window for studying the assembly histories of group- and cluster-mass haloes by using carefully derived proxies based on massive galaxy profiles.

ACKNOWLEDGEMENTS

The authors would like to thank Frank van den Bosch, Sandra Faber, Joel Primack for useful discussions and suggestions.

This material is based upon work supported by the National Science Foundation under Grant No. 1714610.

The authors acknowledge support from the Kavli Institute for Theoretical Physics. This research was also supported in part by National Science Foundation under Grant No. NSF PHY11-25915 and Grant No. NSF PHY17-48958

AL acknowledges support from the David and Lucille Packard foundation, and from the Alfred .P Sloan foundation.

The Hyper Suprime-Cam (HSC) collaboration includes the astronomical communities of Japan and Taiwan, and Princeton University. The HSC instrumentation and software were developed by National Astronomical Observatory of Japan (NAOJ), Kavli Institute for the Physics and Mathematics of the Universe (Kavli IPMU), University of Tokyo, High Energy Accelerator Research Organization (KEK), Academia Sinica Institute for Astronomy and Astrophysics in Taiwan (ASIAA), and Princeton University. Funding was contributed by the FIRST program from Japanese Cabinet Office, Ministry of Education, Culture, Sports, Science and Technology (MEXT), Japan Society for the Promotion of Science (JSPS), Japan Science and Technology Agency (JST), Toray Science Foundation, NAOJ, Kavli IPMU, KEK, ASIAA, and Princeton University.

Funding for SDSS-III has been provided by Alfred P. Sloan Foundation, the Participating Institutions, National Science Foundation, and U.S. Department of Energy. The SDSS-III website is <http://www.sdss3.org>. SDSS-III is managed by the Astrophysical Research Consortium for the Participating Institutions of the SDSS-III Collaboration, including University of Arizona, the Brazilian Participation Group, Brookhaven National Laboratory, University of Cambridge, University of Florida, the French Participation Group, the German Participation Group, Instituto de Astrofísica de Canarias, the Michigan State/Notre Dame/JINA Participation Group, Johns Hopkins University, Lawrence Berkeley National Laboratory, Max Planck Institute for Astrophysics, New Mexico State University, New York University, Ohio State University, Pennsylvania State University, University of Portsmouth, Princeton University, the Spanish Participation Group, University of Tokyo, University of Utah, Vanderbilt University, University of Virginia, University of Washington, and Yale University.

The Pan-STARRS1 surveys (PS1) have been made possible through contributions of Institute for Astronomy; University of Hawaii; the Pan-STARRS Project Office; the

Max-Planck Society and its participating institutes: the Max Planck Institute for Astronomy, Heidelberg, and the Max Planck Institute for Extraterrestrial Physics, Garching; Johns Hopkins University; Durham University; University of Edinburgh; Queen's University Belfast; Harvard-Smithsonian Center for Astrophysics; Las Cumbres Observatory Global Telescope Network Incorporated; National Central University of Taiwan; Space Telescope Science Institute; National Aeronautics and Space Administration under Grant No. NNX08AR22G issued through the Planetary Science Division of the NASA Science Mission Directorate; National Science Foundation under Grant No. AST-1238877; University of Maryland, and Eotvos Lorand University.

This research makes use of software developed for the Large Synoptic Survey Telescope. We thank the LSST project for making their code available as free software at <http://dm.lsstcorp.org>.

The CosmoSim database used in this research is a service by the Leibniz-Institute for Astrophysics Potsdam (AIP). The MultiDark database was developed in cooperation with the Spanish MultiDark Consolider Project CSD2009-00064.

This research made use of: `STSCI_PYTHON`, a general astronomical data analysis infrastructure in Python. `STSCI_PYTHON` is a product of the Space Telescope Science Institute, which is operated for NASA by Association of Universities for Research in Astronomy (AURA); `SciPy`, an open source scientific tool for Python (Jones et al. 2001); `NumPy`, a fundamental package for scientific computing with Python (Walt et al. 2011); `Matplotlib`, a 2-D plotting library for Python (Hunter 2007); `Astropy`, a community-developed core Python package for astronomy (Astropy Collaboration et al. 2013); `scikit-learn`, a machine-learning library in Python (Pedregosa et al. 2011); `IPython`, an interactive computing system for Python (Pérez & Granger 2007); `sep` Source Extraction and Photometry in Python (Barbary et al. 2015); `palettable`, colour palettes for Python; `emcee`, Seriously Kick-Ass MCMC in Python; `Colossus`, COsmology, haLO and large-Scale StrUcture tools (Diemer 2015).

REFERENCES

- Abazajian K. N., et al., 2009, *ApJS*, **182**, 543
- Aihara H., et al., 2011, *ApJS*, **193**, 29
- Aihara H., et al., 2017b, preprint, ([arXiv:1702.08449](https://arxiv.org/abs/1702.08449))
- Aihara H., et al., 2017a, preprint, ([arXiv:1704.05858](https://arxiv.org/abs/1704.05858))
- Alam S., et al., 2015, *ApJS*, **219**, 12
- Amon A., et al., 2018, *MNRAS*, **477**, 4285
- Astropy Collaboration et al., 2013, *A&A*, **558**, A33
- Axelrod T., Kantor J., Lupton R. H., Pierfederici F., 2010, in Software and Cyberinfrastructure for Astronomy. p. 774015, [doi:10.1117/12.857297](https://doi.org/10.1117/12.857297)
- Baldry I. K., et al., 2018, *MNRAS*, **474**, 3875
- Barbary Boone Deil 2015, sep: v0.3.0, [doi:10.5281/zenodo.15669](https://doi.org/10.5281/zenodo.15669), <http://dx.doi.org/10.5281/zenodo.15669>
- Becker M. R., 2015, preprint, ([arXiv:1507.03605](https://arxiv.org/abs/1507.03605))
- Behroozi P. S., Wechsler R. H., Wu H.-Y., 2013a, *ApJ*, **762**, 109
- Behroozi P. S., Wechsler R. H., Conroy C., 2013b, *ApJ*, **770**, 57
- Behroozi P., Wechsler R., Hearin A., Conroy C., 2018, preprint, ([arXiv:1806.07893](https://arxiv.org/abs/1806.07893))
- Bender R., Kormendy J., Cornell M. E., Fisher D. B., 2015, *ApJ*, **807**, 56
- Benson A. J., 2014, *MNRAS*, **444**, 2599
- Benson A. J., 2017, *MNRAS*, **467**, 3454
- Benson A. J., Bower R., 2010, *MNRAS*, **405**, 1573
- Bernardi M., Meert A., Sheth R. K., Vikram V., Huertas-Company M., Mei S., Shankar F., 2013, *MNRAS*, **436**, 697
- Bernardi M., Meert A., Vikram V., Huertas-Company M., Mei S., Shankar F., Sheth R. K., 2014, *MNRAS*, **443**, 874
- Bernardi M., Meert A., Sheth R. K., Fischer J.-L., Huertas-Company M., Maraston C., Shankar F., Vikram V., 2017, *MNRAS*, **467**, 2217
- Bezanson R., van Dokkum P. G., Tal T., Marchesini D., Kriek M., Franx M., Coppi P., 2009, *ApJ*, **697**, 1290
- Bosch J., et al., 2017, preprint, ([arXiv:1705.06766](https://arxiv.org/abs/1705.06766))
- Bryan G. L., Norman M. L., 1998, *ApJ*, **495**, 80
- Budzynski J. M., Kuposov S. E., McCarthy I. G., Belokurov V., 2014, *MNRAS*, **437**, 1362
- Bundy K., Leauthaud A., Saito S., Maraston C., Wake D. A., Thomas D., 2017, *ApJ*, **851**, 34
- Cappellari M., 2014, LTS_LINEFIT and LTS_PLANEFIT: LTS fit of lines or planes, Astrophysics Source Code Library (ascl:1404.001)
- Cappellari M., et al., 2013, *MNRAS*, **432**, 1862
- Chabrier G., 2003, *PASP*, **115**, 763
- Charlton P. J. L., Hudson M. J., Balogh M. L., Khatri S., 2017, preprint, ([arXiv:1707.04924](https://arxiv.org/abs/1707.04924))
- Clampitt J., et al., 2017, *MNRAS*, **465**, 4204
- Clauwens B., Hill A., Franx M., Schaye J., 2017, *MNRAS*, **469**, L58
- Cleveland W. S., Devlin S. J., 1988, Journal of the American Statistical Association, **83**, 596
- Conroy C., Gunn J. E., 2010a, FSPS: Flexible Stellar Population Synthesis, Astrophysics Source Code Library (ascl:1010.043)
- Conroy C., Gunn J. E., 2010b, *ApJ*, **712**, 833
- Conroy C., van Dokkum P. G., Kravtsov A., 2015, *ApJ*, **803**, 77
- Cooper M. C., Gallazzi A., Newman J. A., Yan R., 2010, *MNRAS*, **402**, 1942
- Cooper A. P., D'Souza R., Kauffmann G., Wang J., Boylan-Kolchin M., Guo Q., Frenk C. S., White S. D. M., 2013, *MNRAS*, **434**, 3348
- Coupon J., et al., 2015, *MNRAS*, **449**, 1352
- Coupon J., Czakon N., Bosch J., Komiyama Y., Medezinski E., Miyazaki S., Oguri M., 2017, preprint, ([arXiv:1705.00622](https://arxiv.org/abs/1705.00622))
- Crain R. A., et al., 2015, *MNRAS*, **450**, 1937
- Croton D. J., et al., 2016, *ApJS*, **222**, 22
- Damjanov I., et al., 2009, *ApJ*, **695**, 101
- Dawson K. S., et al., 2013, *AJ*, **145**, 10
- De Lucia G., Blaizot J., 2007, *MNRAS*, **375**, 2
- DeMaio T., Gonzalez A. H., Zabludoff A., Zaritsky D., Connor T., Donahue M., Mulchaey J. S., 2018, *MNRAS*, **474**, 3009
- Diemer B., 2015, Colossus: COsmology, haLO, and large-Scale StrUcture tools, Astrophysics Source Code Library (ascl:1501.016)
- Diemer B., 2017, preprint, ([arXiv:1712.04512](https://arxiv.org/abs/1712.04512))
- Diemer B., Kravtsov A. V., 2015, *ApJ*, **799**, 108
- Diemer B., More S., Kravtsov A. V., 2013, *ApJ*, **766**, 25
- Driver S. P., et al., 2009, *Astronomy and Geophysics*, **50**, 5.12
- Driver S. P., et al., 2011, *MNRAS*, **413**, 971
- Evrard A. E., 1990, *ApJ*, **363**, 349
- Ferré-Mateu A., Trujillo I., Martín-Navarro I., Vazdekis A., Mezcua M., Balcells M., Domínguez L., 2017, *MNRAS*, **467**, 1929
- Foreman-Mackey D., Hogg D. W., Lang D., Goodman J., 2013, *PASP*, **125**, 306
- Gelman A., Jakulin A., Grazia Pittau M., Su Y.-S., 2009, preprint, ([arXiv:0901.4011](https://arxiv.org/abs/0901.4011))
- Genel S., Genzel R., Bouché N., Naab T., Sternberg A., 2009, *ApJ*, **701**, 2002
- Genel S., et al., 2014, *MNRAS*, **445**, 175
- Giodini S., et al., 2009, *ApJ*, **703**, 982

- Golovich N., Dawson W. A., Wittman D., Ogrean G., van Weeren R., Bonafede A., 2016, *ApJ*, **831**, 110
- Gu M., Conroy C., Behroozi P., 2016, *ApJ*, **833**, 2
- Guo Q., et al., 2011, *MNRAS*, **413**, 101
- Hashimoto T., et al., 2018, *Nature*, **557**, 392
- Hearin A. P., et al., 2017, *AJ*, **154**, 190
- Henriques B. M. B., White S. D. M., Thomas P. A., Angulo R., Guo Q., Lemson G., Springel V., Overzier R., 2015, *MNRAS*, **451**, 2663
- Hill A. R., et al., 2017, *ApJ*, **837**, 147
- Hilz M., Naab T., Ostriker J. P., 2013, *MNRAS*, **429**, 2924
- Hirata C., Seljak U., 2003, *MNRAS*, **343**, 459
- Hoekstra H., 2007, *MNRAS*, **379**, 317
- Hopkins P. F., Cox T. J., Kereš D., Hernquist L., 2008, *ApJS*, **175**, 390
- Huang S., Ho L. C., Peng C. Y., Li Z.-Y., Barth A. J., 2013, *ApJ*, **768**, L28
- Huang S., et al., 2018a, preprint, ([arXiv:1803.02824](https://arxiv.org/abs/1803.02824))
- Huang S., et al., 2018b, *PASJ*, **70**, S6
- Huang S., Leauthaud A., Greene J. E., Bundy K., Lin Y.-T., Tanaka M., Miyazaki S., Komiyama Y., 2018c, *MNRAS*, **475**, 3348
- Hunter J. D., 2007, *Computing In Science & Engineering*, **9**, 90
- Johansson P. H., Naab T., Ostriker J. P., 2009, *ApJ*, **697**, L38
- Jones E., Oliphant T., Peterson P., et al., 2001, SciPy: Open source scientific tools for Python, <http://www.scipy.org/>
- Jurić M., et al., 2015, preprint, ([arXiv:1512.07914](https://arxiv.org/abs/1512.07914))
- Kelly P. L., et al., 2015, *Science*, **347**, 1123
- Kelson D. D., Zabludoff A. I., Williams K. A., Trager S. C., Mulchaey J. S., Bolte M., 2002, *ApJ*, **576**, 720
- Khandai N., Di Matteo T., Croft R., Wilkins S., Feng Y., Tucker E., DeGraf C., Liu M.-S., 2015, *MNRAS*, **450**, 1349
- Kravtsov A. V., 2013, *ApJ*, **764**, L31
- Kravtsov A. V., Vikhlinin A. A., Meshcheryakov A. V., 2018, *Astronomy Letters*, **44**, 8
- Leauthaud A., et al., 2012a, *ApJ*, **744**, 159
- Leauthaud A., et al., 2012b, *ApJ*, **746**, 95
- Leauthaud A., et al., 2017, *MNRAS*, **467**, 3024
- Lin Y.-T., Mohr J. J., 2004, *ApJ*, **617**, 879
- Lin Y.-T., Stanford S. A., Eisenhardt P. R. M., Vikhlinin A., Maughan B. J., Kravtsov A., 2012, *ApJ*, **745**, L3
- Lin Y.-T., Mandelbaum R., Huang Y.-H., Huang H.-J., Dalal N., Diemer B., Jian H.-Y., Kravtsov A., 2016, *ApJ*, **819**, 119
- Liske J., et al., 2015, *MNRAS*, **452**, 2087
- Longobardi A., Arnaboldi M., Gerhard O., Hanuschik R., 2015, *A&A*, **579**, A135
- Lu Y., Mo H. J., Weinberg M. D., Katz N., 2011, *MNRAS*, **416**, 1949
- Lundgren B. F., et al., 2014, *ApJ*, **780**, 34
- Mahdavi A., Hoekstra H., Babul A., Henry J. P., 2008, *MNRAS*, **384**, 1567
- Mandelbaum R., Seljak U., Kauffmann G., Hirata C. M., Brinkmann J., 2006a, *MNRAS*, **368**, 715
- Mandelbaum R., Seljak U., Cool R. J., Blanton M., Hirata C. M., Brinkmann J., 2006b, *MNRAS*, **372**, 758
- Mandelbaum R., et al., 2017, preprint, ([arXiv:1710.00885](https://arxiv.org/abs/1710.00885))
- Mandelbaum R., et al., 2018, *PASJ*, **70**, S25
- Mao Y.-Y., Zentner A. R., Wechsler R. H., 2018, *MNRAS*, **474**, 5143
- Medezinski E., et al., 2018, *PASJ*, **70**, S28
- Miyatake H., et al., 2018, preprint, ([arXiv:1804.05873](https://arxiv.org/abs/1804.05873))
- Miyazaki S., et al., 2012, in *Ground-based and Airborne Instrumentation for Astronomy IV*. p. 84460Z, [doi:10.1117/12.926844](https://doi.org/10.1117/12.926844)
- More S., van den Bosch F. C., Cacciato M., Skibba R., Mo H. J., Yang X., 2011, *MNRAS*, **410**, 210
- Moster B. P., Naab T., White S. D. M., 2018, *MNRAS*, **477**, 1822
- Moustakas J., et al., 2013, *ApJ*, **767**, 50
- Muzzin A., et al., 2013, *ApJ*, **777**, 18
- Nagai D., Kravtsov A. V., Vikhlinin A., 2007, *ApJ*, **668**, 1
- Oke J. B., Gunn J. E., 1983, *ApJ*, **266**, 713
- Oogi T., Habe A., 2013, *MNRAS*, **428**, 641
- Oser L., Ostriker J. P., Naab T., Johansson P. H., Burkert A., 2010, *ApJ*, **725**, 2312
- Oser L., Naab T., Ostriker J. P., Johansson P. H., 2012, *ApJ*, **744**, 63
- Owensworth J. R., Conselice C. J., Mortlock A., Hartley W. G., Almaini O., Duncan K., Mundy C. J., 2014, *MNRAS*, **445**, 2198
- Patel S. G., et al., 2013, *ApJ*, **766**, 15
- Patel S. G., Kelson D. D., Williams R. J., Mulchaey J. S., Dressler A., McCarthy P. J., Shectman S. A., 2015, *ApJ*, **799**, L17
- Pedregosa F., et al., 2011, *Journal of Machine Learning Research*, **12**, 2825
- Peralta de Arriba L., Quilis V., Trujillo I., Cebrián M., Balcells M., 2016, *MNRAS*, **461**, 156
- Pérez F., Granger B. E., 2007, *Computing in Science and Engineering*, **9**, 21
- Pillepich A., et al., 2017, preprint, ([arXiv:1703.02970](https://arxiv.org/abs/1703.02970))
- Pillepich A., et al., 2018a, *MNRAS*, **475**, 648
- Pillepich A., et al., 2018b, *MNRAS*, **475**, 648
- Postman M., et al., 2012, *ApJS*, **199**, 25
- Prat J., et al., 2017, preprint, ([arXiv:1708.01537](https://arxiv.org/abs/1708.01537))
- Qu Y., et al., 2017, *MNRAS*, **464**, 1659
- Reddick R. M., Wechsler R. H., Tinker J. L., Behroozi P. S., 2013, *ApJ*, **771**, 30
- Rodriguez-Gomez V., et al., 2016, *MNRAS*, **458**, 2371
- Rodríguez-Puebla A., Primack J. R., Avila-Reese V., Faber S. M., 2017, *MNRAS*, **470**, 651
- Roediger J. C., Courteau S., 2015, *MNRAS*, **452**, 3209
- Rozo E., Rykoff E. S., 2014, *ApJ*, **783**, 80
- Rykoff E. S., et al., 2014, *ApJ*, **785**, 104
- Schaye J., et al., 2015, *MNRAS*, **446**, 521
- Schlafly E. F., Finkbeiner D. P., 2011, *ApJ*, **737**, 103
- Shan H., et al., 2017, *ApJ*, **840**, 104
- Shirasaki M., Takada M., Miyatake H., Takahashi R., Hamana T., Nishimichi T., Murata R., 2017, *MNRAS*, **470**, 3476
- Simet M., Battaglia N., Mandelbaum R., Seljak U., 2017, *MNRAS*, **466**, 3663
- Singh S., Mandelbaum R., Seljak U., Slosar A., Vazquez Gonzalez J., 2017, *MNRAS*, **471**, 3827
- Somerville R. S., Popping G., Trager S. C., 2015, *MNRAS*, **453**, 4337
- Springel V., 2005, *MNRAS*, **364**, 1105
- Takada M., Hu W., 2013, *Phys. Rev. D*, **87**, 123504
- Tanaka M., et al., 2018, *PASJ*, **70**, S9
- Tenneti A., Mandelbaum R., Di Matteo T., Kiessling A., Khandai N., 2015, *MNRAS*, **453**, 469
- Tinker J. L., et al., 2017, *ApJ*, **839**, 121
- Toft S., et al., 2014, *ApJ*, **782**, 68
- Trujillo I., Ferré-Mateu A., Balcells M., Vazdekis A., Sánchez-Blázquez P., 2014, *ApJ*, **780**, L20
- Umetsu K., et al., 2014, *ApJ*, **795**, 163
- Vikhlinin A., et al., 2009, *ApJ*, **692**, 1033
- Vogelsberger M., et al., 2014, *MNRAS*, **444**, 1518
- Walt S. v. d., Colbert S. C., Varoquaux G., 2011, *Computing in Science and Engg.*, **13**, 22
- Wang L., Weinmann S. M., De Lucia G., Yang X., 2013, *MNRAS*, **433**, 515
- Wechsler R. H., Tinker J. L., 2018, preprint, ([arXiv:1804.03097](https://arxiv.org/abs/1804.03097))
- Wellons S., et al., 2016, *MNRAS*, **456**, 1030
- White S. D. M., Frenk C. S., 1991, *ApJ*, **379**, 52
- Yildırım A., van den Bosch R. C. E., van de Ven G., Martín-Navarro I., Walsh J. L., Husemann B., Gültekin K., Gebhardt K., 2017, *MNRAS*, **468**, 4216
- Yoon Y., Im M., Kim J.-W., 2017, *ApJ*, **834**, 73

- Zentner A. R., Hearin A. P., van den Bosch F. C., 2014, *MNRAS*, **443**, 3044
- Ziparo F., et al., 2016, *A&A*, **592**, A9
- Zu Y., Mandelbaum R., 2015, *MNRAS*, **454**, 1161
- Zu Y., Mandelbaum R., 2016, *MNRAS*, **457**, 4360
- van Dokkum P. G., et al., 2008, *ApJ*, **677**, L5
- van Dokkum P. G., et al., 2015, *ApJ*, **813**, 23
- van Uitert E., et al., 2016, *MNRAS*, **459**, 3251
- van der Burg R. F. J., Muzzin A., Hoekstra H., Wilson G., Lidman C., Yee H. K. C., 2014, *A&A*, **561**, A79
- van der Wel A., et al., 2014, *ApJ*, **788**, 28

APPENDIX A: M_{vir} TRENDS OF KEY PREDICTIONS IN THE `UniverseMachine` MODEL

As explained in §5.3, besides M_{vir} , `ASAP` model also relies on three key predictions from the special version of `UniverseMachine` model used in this work:

(i) δ_{cen} : the ratio between the stellar mass of central galaxy and the total stellar mass within the halo. This parameter reflects the “dominance” of central galaxy in the halo. It is determined by the complex merger history of both the halo and the central galaxy.

(ii) δ_{ins} and δ_{exs} : the fractions of stellar mass in the *in situ* and *ex situ* components for each galaxy. They are determined by both the star-formation and mass-assembly history of each galaxy in the halo.

In Fig A1, we visualize their relationships with M_{vir} . On the left side, we show that δ_{cen} slowly decrease with M_{vir} , suggesting that central galaxies become less dominated in more massive halos. Meanwhile, this relation has a significant scatter, especially for halos with $\log_{10}(M_{\text{vir}}/M_{\odot}) \leq 14.0$. The scatter of δ_{cen} at fixed M_{vir} dominates the scatter of the SHMR predicted by our `ASAP` model, although it is yet to learn whether such large scatter is realistic.

On the right side of Fig A1, we demonstrate that the *in situ* (*ex situ*) mass fraction rapidly decreases (increases) with M_{vir} , which is consistent with results from recent hydrodynamic simulations.

APPENDIX B: PERFORMANCE OF M_{vir} ESTIMATORS

As mentioned in §6.4, we attempts to assign M_{vir} to massive galaxies in HSC surveys by comparing the observed aperture stellar masses to the ones predicted by the best-fit `ASAP` model. Here, we briefly demonstrate the performances of two M_{vir} estimators here: the random forest regressor and the 2-D $M_{\star}^{\text{max}}-M_{\star}^{10}-M_{\text{vir}}$ scaling relation. The `Jupyter` notebook used for M_{vir} predictions is available here: [🔗](#).

For the random forest regressor, we use the `RandomForestRegressor` from the `scikit-learn` Python package. We choose to use 20 estimators and mean absolute error criteria. We train the random forest regressor using the predicted M_{\star}^{Max} and M_{\star}^{10} of *central* galaxies from the best-fit `ASAP` model, then validate it using a realization of the `ASAP` model with parameters slightly deviated from the best-fit values. On the left side of Fig B1, we visualize the performance of this estimator across the aperture stellar mass plane. We choose to use $(\log M_{\text{vir}}^{\text{predict}} - \log M_{\text{vir}}^{\text{true}})/\sigma_{\log M_{\text{vir}}^{\text{true}}}$ to

test the accuracy of the prediction where $\sigma_{\log M_{\text{vir}}^{\text{true}}}$ is the scatter of M_{vir} in each 2-D bin of aperture masses. As expected, the random forest regressor can easily capture the detailed trend of M_{vir} over the 2-D aperture stellar mass plane.

Meanwhile, we have shown the best-fit 2-D $M_{\star}^{\text{max}}-M_{\star}^{10}-M_{\text{vir}}$ scaling relation in §6.4. We visualize its accuracy on the right side of Fig B1. As one can see, this simple scaling relation can still capture the main M_{vir} trend over the regions that are occupied by most HSC galaxies (highlighted by contours). Although the M_{vir} predicted by this 2-D scaling relation starts to show deviations compared to true values at the edges of the aperture stellar mass relation, the systematic differences are still comparable to the scatters of M_{vir} in these bins.

In the next paper of this series, we will be looking for more reliable way to predict M_{vir} based on the stellar mass distributions of massive galaxies and improved version of `ASAP` model. We will also directly test these predictions using HSC weak lensing calibrations.

This paper has been typeset from a $\text{\TeX}/\text{\LaTeX}$ file prepared by the author.

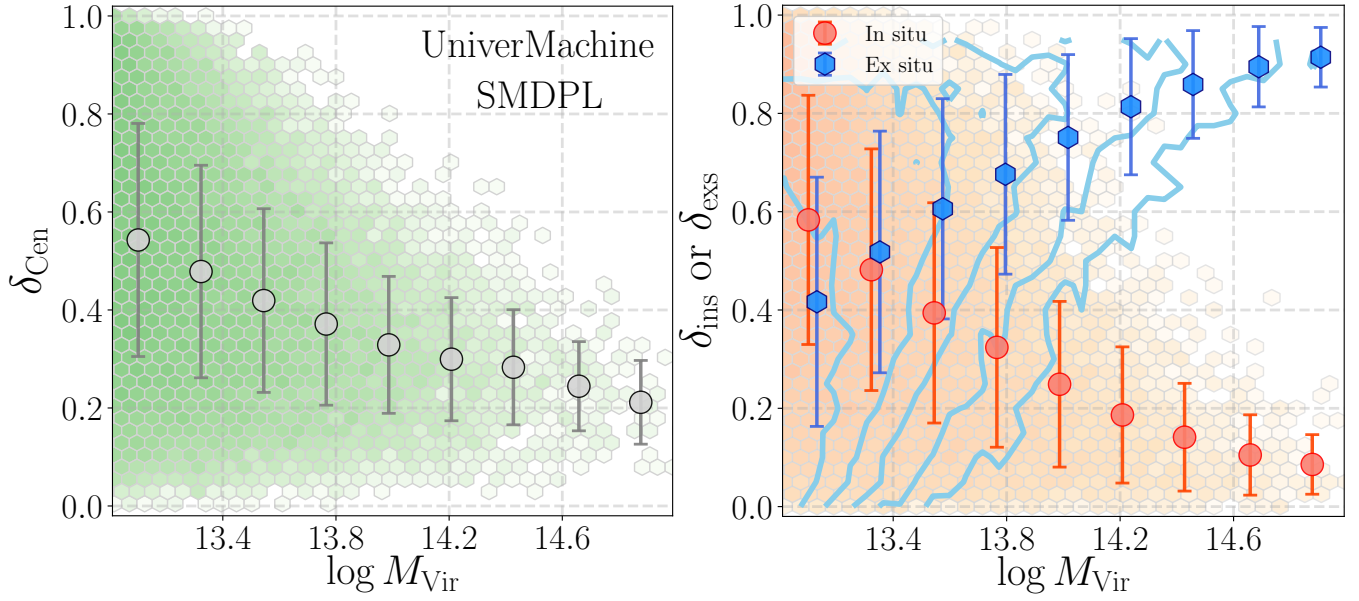


Figure A1. Distributions of M_{\star} fraction of central galaxy ($M_{\star}^{\text{cen}}/M_{\star}^{\text{all}}$) and its dependence on M_{vir} . Color shows the number density of galaxies in log-scale. The median central mass fractions in a series of M_{vir} bins are highlighted using grey circles along with the $1\text{-}\sigma$ scatter in each bin. The shaded region on the left side is for the M_{vir} range ignored in this work. The *Jupyter* notebook for this figure is available here: [📄](#)

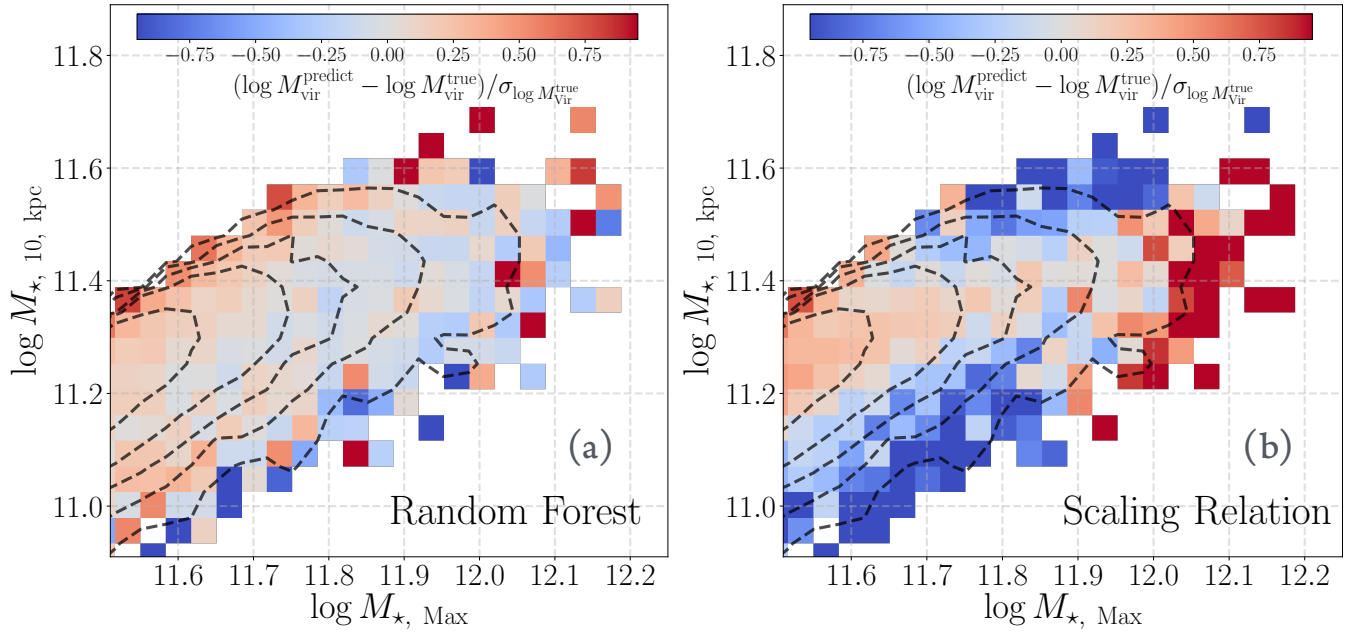


Figure B1. Evaluation of two different M_{vir} predictors based on the halo mass trend over the aperture mass plane. The left panel is for the random forest regressor and the right side is for the $M_{\star}^{\text{max}}\text{-}M_{\star}^{10}\text{-}M_{\text{vir}}$ scaling relation. On both figures, the color indicates the relative differences between the predicted M_{vir} and the true values from the *UniverseMachine* model. Regions occupied by most observed HSC galaxies are highlighted using grey contours. The *Jupyter* notebook for this figure is available here: [📄](#)